Quarkeigenschaften, Topologie und Confinement im Rahmen der Gittereichtheorie

DIPLOMARBEIT
von
Daniel-Jens Kusterer

Institut für Theoretische Physik
Eberhard-Karls-Universität Tübingen

März 2004

Zusammenfassung

Die Theorie der starken Wechselwirkung, die sog. Quanten Chromo Dynamik (QCD), ist eine relativistische Quantenfeldtheorie, und ist, wie die QED, eine Eichtheorie, allerdings mit der Eichgruppe SU(3). Durch die unendliche Zahl an Freiheitsgraden in einer Quantenfeldtheorie kommt es zu Divergenzen, welche durch eine sog. Regularisierung behoben werden müssen. Der hierfür weit verbreitete Ansatz ist die Störungstheorie. Allerdings ist der störungstheoretische Ansatz im Niederenergiebereich stark wechselwirkender Theorien nicht einsetzbar, wodurch Phänomene wie der Farbeinschluss oder die Brechung der chiralen Symmetrie nicht mit störungstheorethischen Methoden behandelbar sind. Der Farbeinschluss, auch (Colour) Confinement genannt, ist die Tatsache, dass keine freien Teilchen, die eine nichtverschwindende Farbladung tragen, experimentell beobachtet werden können. Chirale Symmetrie ist die Symmetrie zwischen links- und rechtshändigen Quarks, welche im Grundzustand des QCD-Vakuums spontan gebrochen ist. Pionen, die Goldstone Bosonen dieser spontanen Symmetriebrechung, besitzen als nahezu masselose Teilchen eine herausragende Rolle im Teilchenspektrum. Da sich diese Arbeit mit dem Confinement-Problem beschäftigt, wird ein nicht-störungstheoretischer Zugang benötgt. Die Gittereichtheorie, in der die QFT durch Einführen eines Raum-Zeit-Gitters regularisiert wird, bietet einen direkten Zugang zum nichtpertubativen Regime. Zugleich ist es der derzeit einzige nicht-störungstheoretische Zugang, der frei von unkontrollierbaren Näherungen ist. Alle Untersuchungen für diese Arbeit werden mit Hilfe der Gittereichtheorie vorgenommen. Gluonen, die Austauschteilchen der starken Wechselwirkung, werden in der Theorie durch Eichfelder dargestellt. Diese Eichfelder können durch ihre topologische Ladung, auch Windungszahl genant, klassifiziert werden. Die Topologie der Eichfelder kann mit, z.B. semi-klassischen, Objekten, wie Instantonen, verknüpft sein. Diese Diplomarbeit untersucht solche topologische Objekte im Rahmen der Gittereichtheorie. Ein besonderer Augenmerk wird dabei auf zwei Arten solcher Objekte gelegt, Instantonen im ersten Teil der Arbeit und Vortizes im zweiten Teil.

Genauer gesagt beschäftigt sich der erste Teil dieser Arbeit mit der Wahrscheinlichkeitsdichte von niedrigen Eigenmoden des hermitschen Wilson-Dirac Operators $H(\kappa) = \gamma_5 D_{\mathrm{W}}(\kappa)$ und ihrer Verbindung zur Topologie. Position und Ausdehnung der Eigenmodendichte und der topologischen Ladungsdichte sowie der Wirkungsdichte werden verglichen. Diese Vergleiche werden für SU(3) Hintergrundfelder, die mit einem Monte-Carlo Verfahren hergestellt wurden, und für Hintergrundfelder, auf die ein einzelnes Instanton gesetzt wurde, gemacht. Position und Ausdehnung der Eigenmodendichte und der topologischen Ladungsdichte werden durch das Anfitten eines Instanton Modells verglichen. Topologische Ladungsdichte, Wirkungsdichte und Eigenmodendichte werden als 3-D Schnitt durch das 4-D Raumzeitgitter visualisiert und geplottet. Es wird gezeigt, dass für nackte Quarkmassen

m_0 mit $0 \leq m_0 \leq 2$ nicht nur Nullmoden, sondern alle niedrigen Eigenmoden des hermitschen Wilson-Dirac Operators eine starke Korrelation mit topologischen Objekten zeigen. Diese Objekte können Instantonen, oder topologische Fluktuationen sein. Es wird gezeigt, dass Eigenmoden heisser SU(3) Konfigurationen für den gesamten Bereich von m_0 starke Korrelationen mit Objekten aufweisen, die in der topologischen Ladungsdichte nach zwölf Kühlschritten eindeutig identifiziert werden können. Objekte, die in der Eigenmodendichte gefunden werden haben ungefähr die selbe Grösse wie die zugehörigen Objekte in der topologischen Ladungsdichte. Für solche heissen SU(3) Konfigurationen findet man, dass mindestens die niedrigsten zwanzig Eigenmoden starke Korrelation zur Topologie aufweisen. Dabei kann nur eine sehr schwache Aufweitung der Korrelation festgestellt werden. Bei der Betrachtung von Eigenmoden gekühlter SU(3) Konfigurationen stellt man, im Vergleich zu heissen Konfigurationen, einen Unterschied fest. Nur Eigenmoden für kleine Massen m_0 weisen die beschriebenen starken Korrelationen auf. Für Eigenmoden für grössere Massen m_0, aber $m_0 \leq 2$, werden diese Korrelation zur Topologie sehr schwach, d.h. die Eigenmoden sind nur noch schwach lokalisiert.

Im zweiten Teil dieser Arbeit wird die Verbindung zwischen Zentrumsvortizes und Confinement untersucht. Um dünne Zentrumsvortizes zu identifizieren sind mehrere Schritte notwendig. Zuerst werden im Monte-Carlo Verfahren mit 3-Loop verbesserter Wirkung hergestellte SU(3) Hintergrundfelder in die maximale Zentrumseichung (MCG) gebracht. Dazu wird die *mesonische* Eichbedingung maximiert. Für die eichfixierten Links $U_\mu^\Omega(x)$ wird dann das Zentrumselement $Z_\mu(x)$ gefunden, welches den Link am besten repräsentiert. Mit diesen Zentrumselementen wird der Zentrumsfluss durch jede Plaquette berechnet und somit definiert, ob ein Vortex die Plaquette durchstösst. Die Unabhängigkeit der physikalischen Vortexdichte von Gitterabstand a wird gezeigt. Dies legt nahe, dass die derart identifizierten Vortizes physikalisch sind. Um den Einfluss von Zentrumsvortizes auf das Farbconfinement zu testen wird das statische Quark-Antiquarkpotential für volle SU(3) Konfigurationen, für Konfigurationen die nur Vortizes enthalten und für Konfigurationen aus denen die Vortizes entfernt wurden, berechnet. Der Einfluss der Eichbedingung auf dieses Verfahren wird durch die Implementierung der *idealen* Zentrumseichung (ICG), als Vergleich zur maximalen Zentrumseichung, getestet. Es wird gezeigt, dass eine Theorie, die nur Zentrumsvortizes besitzt, Confinement aufweist, wohingegen die entsprechende Theorie aus der die Vortizes entfernt wurden kein Confinement mehr aufweist, also die Stringspannung verschwindet. Die Stringspannung für die Vortextheorie beträgt aber nur ungefähr 62% der vollen SU(3) Stringspannung für MCG Vortizes und nur ungefähr 58% für ICG Vortizes. Daher wird vorgeschlagen, dass die *mesonische* Eichbedingung eine gute Näherung für die *ideale* Eichbedingung ist. Desweiteren werden Vorschläge gemacht wie das Rätsel der fehlenden 40% Stringspannung gelöst werden könnte. Diese Vorschläge beinhalten eine mathematische Erklärung und die Laplace Zentrumseichung.

Quark properties, topology and confinement from Lattice Gauge Theory

Acknowledgments

Abstract

In this diploma thesis different topological objects are examined using Lattice Gauge Theory. As a first part the probability density of low-lying eigenmodes of the hermitian Wilson-Dirac operator $H(\kappa) = \gamma_5 D_{\mathrm{W}}(\kappa)$ and its connection to topology is examined. Comparisons in position and size between eigenvectors, topological charge and action density are made. This is done for standard Monte-Carlo generated SU(3) background fields and for single instanton background fields. Both hot and cooled SU(3) background fields are considered. Sizes and positions of eigenmode and topological charge density are compared by fitting an instanton model. Visualisations of topological charge, action and eigenmode densities are provided. It is shown that not only zero modes, but all low-lying eigenmodes of the hermitian Wilson-Dirac operator are strongly correlated to topological objects for bare quark masses m_0 with $0 \leq m_0 \leq 2$. These objects can be instantons or topological fluctuations. For all m_0, eigenmodes of hot SU(3) configurations are seen to display strong correlations to objects, which can be identified in the topological charge density of twelve sweep cooled configurations. The objects in the eigenmode density are found to have roughly the same size as the corresponding topological object. For such configurations the twenty lowest eigenmodes are seen to have strong correlations to topological objects with only little broadening for higher eigenmodes. Eigenmodes of twelve sweep cooled configurations are found to have a different behaviour. They are strongly correlated to topological objects for small m_0 and weakly correlated with such objects for large m_0.

In the second part the connection between center vortices and confinement is examined. To identify thin center vortices Monte-Carlo generated SU(3) background fields are gauge fixed to Maximal Center Gauge (MCG) by maximising the *mesonic* gauge condition. The background fields considered are created with a three-loop improved action. Vortices are then identified by finding the closest center element $Z_\mu(x)$ for each link $U_\mu(x)$ and calculating the center flux for each plaquette. It is shown that the vortex density in physical units is independent of the lattice spacing a. This suggests that center vortices identified by MCG gauge fixing are physical. To test the confining properties of center vortices the static quark-antiquark potential is considered for full SU(3), vortex-only and vortex removed configurations. The influence of the gauge condition on this procedure is tested by implementation of the *ideal* gauge condition (ICG) as a comparison. It is shown that a vortex-only theory is confining, whereas the corresponding vortex-removed theory is non-confining, i.e. the string tension vanishes. The string tension of the vortex-only theory is found to be roughly 62% of the full SU(3) string tension for MCG vortices and 58% for ICG vortices. It is suggested that the *mesonic* gauge condition is a good approximation to the *ideal* gauge condition. Ideas of how to solve the missing string tension puzzle are presented.

What songs the Syrens sang, or what name Achilles assumed when he hid himself among women, although puzzling questions, are not beyond all conjecture.

<div align="right">Sir Thomas Brown</div>

Contents

Chapter 1

Introductory thoughts

The standard model of todays particle physics includes all we know about the fundamental forces of electromagnetism, the weak and the strong interaction. It is a (special) relativistic Quantum Field Theory (QFT) and has been tested in great detail for energies up to approximately 100 GeV. Like QED it is a gauge theory, but with the gauge group $SU(3)_c \otimes SU(2)_L \otimes U(1)_Y$.

Creating a Quantum Field Theory, which means quantising a field theory with its infinitely many degrees of freedom is not a straightforward issue. Too naive approaches lead to divergent results. In the process of creating a meaningful QFT some kind of regularisation scheme has to be introduced. Usually this is done by introducing an ultra-violet cut-off. However this has to be done in a gauge invariant way and the integration measure of the fields in the path integral has to be specified, as well. There are different approaches to this regularisation issue. Maybe the oldest one being the perturbative approach. In Perturbation Theory the path integral is expanded in orders of the coupling constant. The resulting Feynman diagrams are then regularised order by order. This perturbative approach gives impressive results, especially in weakly interacting theories like QED. E.g. the anomalous magnetic moment of the electron is the theoretically best understood quantity in physics.

However, perturbation theory has an important problem. It is just an asymptotic expansion, the sum of all orders diverges. By using this approach we therefore can not define the theory beyond perturbation theory. Perturbation theory, however, is useless in the low energy regime of strongly coupled theories, like QCD. Nevertheless there are important phenomena, like confinement, chiral symmetry breaking or the Higgs mechanism, which can only be studied appropriately by a non-perturbative approach. Confinement, or more exact colour-confinement is the fact, that no free particles having colour-charge can be found in the physical spectrum.

Colour-charge can be understood as some kind of generalised electric charge. All asymptotic particle states found in nature are colour singlets and either consist of a quark-antiquark pair (mesons) or three quarks (baryons)[1]. No proof from first principles of this experimental fact has been found up to now. Chiral symmetry is the symmetry between left- and right-handed quarks. It is spontaneously broken by the QCD groundstate, which follows from $< 0|\bar{Q}Q|0 >=< 0|\bar{Q}_L Q_R + \bar{Q}_R Q_L|0 >\neq 0$. The confinement mechanism will be studied in this work, thus a different approach to regularize the QFT than perturbation theory is needed to carry out this study. Introducing a space-time lattice by replacing the space-time continuum with a mesh of discrete lattice points is a clean way of doing this. This lattice theory is not an approximation to the continuum, but rather defines the theory in the critical limit of vanishing lattice spacing. To recover continuum physics the theory has to be renormalized by sending the lattice spacing, usually denoted a, to zero while adjusting the bare couplings accordingly. The lattice regularisation, usually called Lattice Gauge Theory (LGT) respects local gauge symmetries. The space-time symmetries violated through the introduction of the lattice are recovered in the continuum limit. All calculations for this work are carried out with this beautiful tool of LGT[2].

Lattice gauge theory is, of course, not free of problems. Fermion doubling, Gribov copies and explicit chiral symmetry breaking, just to mention some. The fermion doubling problem arises when latticising the free Dirac field. Due to zeros of the polarisation tensor at the edges of the Brillouin zone the continuum limit gives rise to 2^d species of fermions, with d being the number of dimensions. To obtain the correct continuum limit, these extra species must be eliminated. But there is one subtelity, the "no-go" theorem found by Nielsen and Ninomiya [3]. It states that a lattice fermion action can not simultaniously obey locality, translational invariance, chiral symmetry and be doubler free. Different doubler free lattice actions have been developed which then break one of the other three constraints. The standard Wilson action, for example, explicitly breaks chiral symmetry. A method for creating a doubler free lattice action obeying chiral symmetry, which is important for studying chiral symmetry on the lattice, is to have a moderate non-locality. The overlap action [4, 5], see sec. 1.1, is an example of a doubler free action not explicitly breaking chiral symmetry. Gribov ambiguities arise if the gauge fixing procedure is not unique, meaning that for each configuration satisfying the gauge condition there are other, gauge equivalent configurations, the Gribov copies, also satisfying the gauge condition. However, there are gauges, e.g. the Laplacian

---

[1] First evidence for exotic states, i.e. five quark states, have been found recently. Nevertheless these are colour singlets, too.

[2] For a thorough introduction to LGT see the excellent books by Montvay, Münster [1] and Rothe [2].

gauge, which do not suffer from Gribov copies, or apropriate methods for data analysis have to be used. Being able to do accurate calculations even on coarse lattices is important for saving computer time. For this purpose so called improved actions have always been developed since the introduction of LGT. Such actions suppress lattice discretisation errors to higher orders in a. This allows the use of coarse lattice for calculations. Improved actions need to have an enhanced rotational symmetry, physical results, e.g. the quark-antiquark potential, should have the same values, if computed from diagonal or straight elements of the lattice.

Topological excitations of the QCD vacuum are believed to have significant influence on non-perturbative phenomena like chiral symmetry breaking and confinement. Gaining more insight into these phenomena is therefore directly connected to examinations of topology. Different possibilities for topological objects exist on the lattice, but I will concentrate on two - probably the most prominent ones - namely instantons, or instanton like objects, and vortices. In the next two subsections I will describe why and how I consider these topological objects.

1.1   Low-lying eigenmodes and instantons

It is generally believed that topological objects like instantons are connected to spontaneous chiral symmetry breaking. This is due to the fact that instantons and anti-instantons could create a number of small non-zero eigenvalues of the Dirac-matrix [6]. With the Banks-Casher relation [7] this leads to spontaneous chiral symmetry breaking. Meaningful exploration of chiral symmetry on the lattice is only possible with an operator that does not break chiral symmetry explicitly. Naturally one is therefore interested in the connection of such an operator, e.g. the overlap operator, and topology. The overlap operator is defined by

$$D_{\mathrm{ovlp}} = \frac{1 + \gamma_5 \epsilon(H)}{2}, \qquad \epsilon(H) = \frac{H}{\sqrt{H^2}}. \tag{1.1}$$

with H being a hermitian Dirac operator called the "kernel" of the overlap formalism. DeGrand [8] found such a connection by examining zero modes of the overlap operator. These are strongly localised, which was shown in previous works by Edwards, Smith and Jansen [9, 10, 11, 12], as well as correlated to topological objects, which could be instantons. Guided by these ideas I examined to which extend similar properties are already manifested at the kernel level of the overlap formalism [13].

As an overlap kernel, and thus as the operator used for the calculations, I utilised the hermitian Wilson-Dirac operator $H(m_0) = \gamma_5 D_{\mathrm{W}}$. This operator is based on

the standard Wilson-Dirac operator D_{W} and is defined in sec. 2.3.1. The main interest lies in the localisation of eigenmodes. For this purpose the eigenvalue problem $D_{\mathrm{W}}\psi(x) = \lambda\psi(x)$ is solved for the first four low-lying eigenvalues. To get an idea how the behaviour of the eigenmodes changes at the edges of the physical region of the overlap formalism some further points just outside the physical region are calculated as well. The physical region of the overlap operator in terms of the bare quark mass m_0 is given by $0 \leq m_0 \leq 2$. Actual calculations are performed with the hopping parameter κ, which is related to the bare quark mass m_0 by

$$\kappa = (8 - 2m_0)^{-1}. \tag{1.2}$$

Thus the region where the actual calculations are performed is the κ-region starting slightly below the critical value of $\kappa = \kappa_{\mathrm{c}}$ and extending slightly beyond the point where doublers appear in the continuum limit of the overlap formalism. I consider $0.115 \leq \kappa \leq 0.26$ at tree level. Since the critical κ-value shifts from its free field value of 0.125 to some higher value for non-zero gauge coupling, one has to adjust the κ-range accordingly.

Eigenmodes are found by an accelerated conjugate gradient routine [14] which is further improved by using dynamic state renormalisation. The major advantage of a conjugate gradient algorithm besides its almost perfect parallel structure is that it yields not only eigenvalues with appropriate degeneracies, but eigenvectors, as well. For selected κ-values up to 20 eigenmodes are calculated. In the following, the phrase "low-lying eigenmodes" should be understood to mean eigenmodes corresponding to the low-lying eigenvalues.

In order to examine localisations of calculated eigenmodes I plot the probability density $\rho(x) = \parallel \psi(x) \parallel^2$ for three dimensional cuts through the lattice. For comparison the action density as well as the topological charge density for the appropriate configuration are plotted in the same way. The calculations are made on $8^3 \times 16$, 16^4 and $16^3 \times 32$ lattices with anti-periodic fermion boundary conditions in the time direction. On the $8^3 \times 16$ lattice the correlation of low-lying eigenmodes with a single instanton configuration and standard Monte-Carlo generated SU(3) background fields are tested. For the latter background fields hot, 5-sweep and 12-sweep cooled configurations are considered. Calculations on the larger lattices are to verify the conclusions obtained from the smaller lattice. An instanton model, more closely described in sec. 2.3.2, is used to quantify the results further.

1.2   Why consider vortices?

Confinement, one of these problems in QCD requiring a non-perturbative treatment, is still not understood from first principles, in spite of people trying to find

a derivation ever since the introduction of QCD as the fundamental theory of hadronic physics. The confinement problem is such an interesting topic, that the *Clay Mathematical Institute*[3] offered a one million dollar prize for solving it. The official problem description by Jaffe and Witten is found in [15]. There have been quite a few proposals during recent years in how to solve the mystery, that no free particles with a non-zero colour charge are found in nature, including work in the field of string/M-theory and lattice gauge theory. On the LGT side most proposals see the reason for confinement in topological objects, including instantons, monopoles and vortices. Working on the confinement problem using instantons provides a nice connection between localisations of low-lying eigenmodes and the confinement problem. However, center vortices, as first suggested by 't Hooft [16] in the early 1980ies, seem to be the more promising candidates for solving the confinement puzzle. Recent numerical simulations in SU(2) LGT [17, 18, 19, 20, 21] and SU(3) LGT by Faber, Langfeld and Stack [22, 23, 24] showed very interesting results and made center vortices a prime ansatz for work on the confinement problem. Center vortices are closed areas, in four dimensions, or closed loops, in three dimensions, carrying a quantised magnetic flux. To identify center vortices one looks at Wilson-loops. Note that my definition of a Wilson-loop includes the trace, see appendix A.2. The quantised flux of a center vortex imprints a factor of a gauge group center element on the Wilson-loop, see sec. 2.4. In the case of an SU(N) gauge group the center elements are $Z = \exp\left(i\frac{2\pi}{N}m\right)\mathbb{1}$, with $-\frac{N}{2} < m \leq \frac{N}{2}$ and $m \in \mathbb{Z}$.

Some new strong evidence that center degrees of freedom indeed are important will be presented in this work. See sec. 4.1 for details. These new results show that the phase distribution of large Wilson-loops for full lattice configurations is strongly peaked at values $\phi = -\frac{2\pi}{3}, 0, \frac{2\pi}{3}$ corresponding to center fluxes of $m = -1, 0, 1$.

But how do I show that the center vortex ansatz, or any other idea tells us something about confinement?

In order to find out if certain degrees of freedom have a confining capability, one needs to reduce the pure Yang-Mills theory under retention of its confining capability. On the lattice the confining capability of a theory is best tested by calculating the static quark-antiquark potential. If it rises linearly for large distances the theory is confining, if the potential is flat for large distances the theory is non-confining. The degrees of freedom we are interested in must obey at least three criteria:

- (i) the degrees of freedom are sensible in the continuum limit,

- (ii) they are connected to confinement,

- (iii) they are weakly interacting.

---

[3]http://www.claymath.org
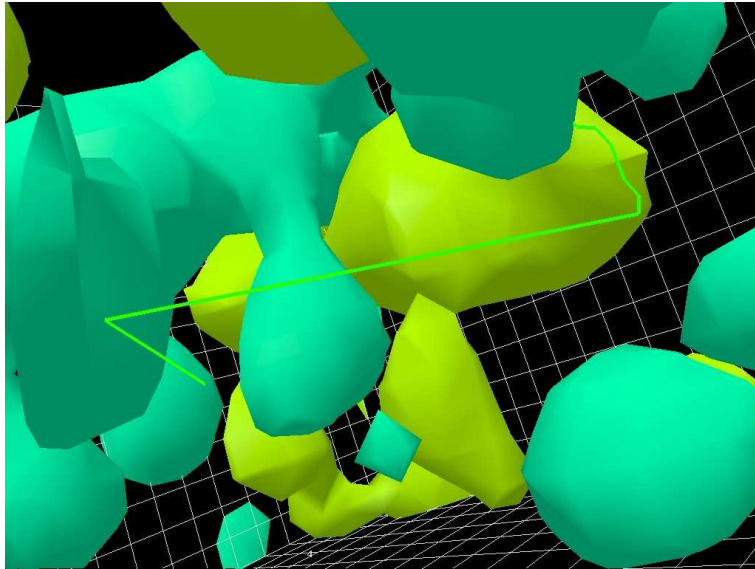
Figure 1.1: A thin vortex visualised in a 3-D cut through the 4-D lattice, with topological charge density.

Criterium (i) is obvious, as one would like to have physical degrees of freedom. Criterium (ii) should be obvious, as well. One would like to explain confinement, thus the degrees of freedom one is interested in using for this explanation should be connected to the concept of confinement. Criterium (iii) follows from the physical intuition, as one would like to describe a theory with weakly interacting degrees of freedom. For center degrees of freedom Criterium (ii) is always fullfilled, as one definition of the confinement problem involves the gauge group center. For more on this definition see the excellent review by Greensite [25]. I will show in this work that the other two criteria are satisfied in the center vortex picture, as well. The random vortex model with randomly distributed percolating vortices satisfies the criteria and is able to describe a confining static quark-antiquark potential. Thus if the vortex texture found in the lattice simulations performed for this work, is similar or close to the random vortex model, one can assume that the criteria are satisfied.

A technique for reducing the pure Yang-Mills theory to a center vortex theory has been proposed by DelDebbio *et al.* [20, 26] based upon gauge fixing to the so called maximal center gauge (MCG), followed by center projection $SU(N) \rightarrow Z_N$. Vortices appear as dynamical degrees of freedom of the Z_N gauge theory. For SU(2) gauge theory it has been shown, firstly by [20, 26], that a Z_2 gauge theory reproduces a good deal of the string tension and a theory where the Z_2 vortices have been projected out has no more confining capability. Throughout this work I

will call the Z_N gauge theory a vortex-only theory and the theory with the vortices projected out a vortex-removed theory. When not explicitly mentioning anything else, vortices are to be understood as thin-, or p-vortices. In this diploma thesis I am going to present further work on the vortex picture in SU(3) gauge theory, for which a three-loop improved action is used. The improved lattice configurations used in this work were kindly provided by the CSSM[4] lattice collaboration. Problems connected to the MCG vortices in SU(3) LGT and ideas how to solve them, will be presented, as well. These ideas include an *ideal* center gauge, where the gauge transformation best in bringing the full SU(3) configuration close to the vortex texture, is found. Results for this *ideal* center gauge are then compared to MCG results.

1.3   Structure

This work is organised as follows. Following this introductory part there is a part explaining the technique, where in sec. 2.1 improved action and topological charge operators will be described. A short overview of the simulation parameters follows in sec. 2.2. Sec. 2.3 gives a introduction to the hermitian Wilson-Dirac operator and technical details of the low-lying eigenmodes and instanton issue. Algorithms for maximal center gauge fixing and vortex identification are described in sec. 2.4, followed by the static quark-antiquark potential, an important tool to show whether a theory is confining or not, in sec. 2.5.
The next part is then dedicated to the numerical results. Within this part chapter 3 gives detailed results for the low-lying eigenmode and instanton examination, whereas results for the center vortex picture of confinement are presented in chapter 4. The last chapter of this work will be left for the conclusions and outlook.

---

[4]Special Research Centre for the Subatomic Structure of Matter
http://www.physics.adelaide.edu.au/cssm

Chapter 2

Lattice techniques

2.1 Improved lattice actions and topological charge

2.1.1 The lattice action

Accurate lattice calculations at small lattice spacings require a high computational effort. To increase accuracy and reduce computer time people have always tried to improve the standard "naive" lattice fermion action, by identifying and algebraically removing discretisation errors, ever since the introduction of the "Wilson Term" [27]. The standard Wilson action

$$S_{\mathrm{W}} = \bar{\psi}(x) \left[\sum_{\mu} \left(\gamma_\mu \nabla_\mu - \frac{1}{2} r a \Delta_\mu \right) + m \right] \psi(x), \tag{2.1}$$

where ∇_μ and Δ_μ are the standard covariant first and second order lattice derivatives,

$$\nabla_\mu \psi(x) = \frac{1}{2a} \left[U_\mu(x)\psi(x+\mu) - U_\mu^\dagger(x-\mu)\psi(x-\mu) \right],$$

$$\Delta_\mu \psi(x) = \frac{1}{a^2} \left[U_\mu(x)\psi(x+\mu) + U_\mu^\dagger(x-\mu)\psi(x-\mu) - 2\psi(x) \right],$$

explicitly breaks chiral symmetry at $\mathcal{O}(a)$. To reliably extrapolate continuum physics computations have to be performed on fine lattices, which are computationally very expensive. Scaling properties of this action at finite lattice spacing a can be improved by introducing any number of higher dimensional operators. Such operators vanish in the continuum limit and are therefore called irrelevant. The first action to use this method is the so called Sheikholeslami-Wohlert (clover) action [28], which introduces an additional irrelevant dimension-five operator to the standard Wilson [27] quark action,

$$S_{\mathrm{SW}} = S_{\mathrm{W}} - \frac{i a C_{\mathrm{SW}} r}{4} \bar{\psi}(x) \sigma_{\mu\nu} F_{\mu\nu} \psi(x), \tag{2.2}$$

where C_{SW} is the clover coefficient which can be tuned to remove $\mathcal{O}(a)$ errors.

$$C_{\mathrm{SW}} = \begin{cases} 1 & \text{at tree-level} , \\ 1/u_0^3 & \text{mean-field improved} , \end{cases} \qquad (2.3)$$

with the tadpole improvement factor u_0 which corrects for the quantum renormalisation of the operators. C_{SW} can be tuned nonperturbatively to all powers in g^2. Such non-perturbative (NP) $\mathcal{O}(a)$ improvement [29] shows excellent scaling.

However, there are drawbacks to the clover action which make further improvements necessary. One of the problems are the associated exceptional configurations. In such configurations the quark propagator encounters singular behavior as the quark mass becomes small, therefore making meaningful measurements impossible. In practice, the use of coarse lattices is prevented by this, which means lattice spacings have to be smaller than $a = 0.18$ fm for actual calculations. A second drawback is the plaquette version of $F_{\mu\nu}$ commonly used in eq. 2.2. It has large $\mathcal{O}(a^2)$ errors, which can lead to errors of the order of 10% in the topological charge, even on smooth configurations.

In order to perform faster and more accurate calculations there is still a need for further improvements. Such improvements in the lattice action and topological charge operator will be described in the next two sections.

Improving the action

If the Wilson action is constructed using a linear combination of the plaquette and the average of the 1×2 and 2×1 rectangular Wilson loops $\mathcal{O}(a^2)$ errors can be eliminated. Higher order error terms can be eliminated with the inclusion of other loops in this method. This was previously used by deForcrand *et al.* [30] to construct an action free from $\mathcal{O}(a^2)$ and $\mathcal{O}(a^4)$ errors by using the five planar Wilson loops

- $L^{(1,1)} = W_{\mu\nu}^{(1\times 1)}$

- $L^{(2,2)} = W_{\mu\nu}^{(2\times 2)}$

- $L^{(1,2)} = \frac{1}{2} \left(W_{\mu\nu}^{(1\times 2)} + W_{\mu\nu}^{(2\times 1)} \right)$

- $L^{(1,3)} = \frac{1}{2} \left(W_{\mu\nu}^{(1\times 3)} + W_{\mu\nu}^{(3\times 1)} \right)$

- $L^{(3,3)} = W_{\mu\nu}^{(3\times 3)}$.

With these a general improved action can be written

$$\begin{aligned} S_{\mathrm{IMP}} = \ & c_1 S(L^{(1,1)}) + c_2 S((2,2)) + c_3 S(L^{(1,2)}) \\ & c_4 S(L^{(1,3)}) + c_5 S(L^{(3,3)}), \end{aligned} \qquad (2.4)$$

where $c_1, \cdots, c_5$ are the improvement factors which Bilson-Thompson, *et al.* [31, 32] find to take the values

$$
\begin{aligned}
c_1 &= (19 - 55c_5)/9 \\
c_2 &= (1 - 64c_5)/9 \\
c_3 &= (640c_5 - 64)/45 \\
c_4 &= 1/5 - 2c_5
\end{aligned}
$$

with c_5 being a free parameter which can be used for tuning the action. Tuning the action means that by setting c_5 to $c_5 = 0$ or $c_5 = 1/10$ contributions towards the general improved action S_{IMP} from $L^{(3,3)}$ and $L^{(1,2)}, L^{(1,3)}$ respectively can be eliminated. In this way a 4-loop and a 3-loop improved action can be created. It is important to note, however, that the 3-loop and 4-loop improved actions are just special cases of the 5-loop improved action and for all choices of c_5 the actions are free from discretisation errors up to and including $\mathcal{O}(a^4)$. The $\mathcal{O}(a^6)$ errors, however, are different which leads to slightly different results for calculations with 3-,4- and 5-loop actions.

2.1.2   The topological charge

The topological charge on the lattice is calculated as the sum of the local topological charge density over all lattice sites,

$$
Q = \sum_x q(x) = \frac{1}{32\pi^2} \sum_x \epsilon_{\mu\nu\rho\sigma} \mathrm{Tr}\left(F_{\mu\nu}(x) F_{\rho\sigma}(x)\right). \tag{2.5}
$$

As the standard definition of $F_{\mu\nu}$ has discretisation errors of order 10%, see above, there are rather large errors in computing the topological charge the standard way. Fortunately the topological charge can be improved in much the same way as the lattice action.

For the standard topological charge I use the traceless definition of $F_{\mu\nu}$ extracted from the consideration of 1×1 plaquettes alone [33]

$$
gF_{\mu\nu} = \frac{-i}{8}\left[\left(W_{\mu\nu}^{(1\times1)} - W_{\mu\nu}^{(1\times1)\dagger}\right) - \frac{1}{3}\mathrm{Tr}\left(W_{\mu\nu}^{(1\times1)} - W_{\mu\nu}^{(1\times1)\dagger}\right)\right], \tag{2.6}
$$

where $W_{\mu\nu}^{(1\times1)}$ is the clover-sum of four 1×1 Wilson loops lying in the μ, ν plane. Note that the tracelessness of the Gell-Mann matrices is enforced by subtracting one-third of the trace of $W_{\mu\nu}^{(1\times1)} - W_{\mu\nu}^{(1\times1)\dagger}$. Although this is the standard definition of $F_{\mu\nu}$ not everyone enforces the tracelessness.

The improved field-strength tensor

To improve the topological charge it is a good approach to improve the field-strength tensor $F_{\mu\nu}$ directly, by analogy with the improvement of the action, and then insert the improved $F_{\mu\nu}$ into the definition of the topological charge (eq. 2.5). To construct the improved field strength-tensor the same five planar Wilson loops as in the construction of the improved action, see 2.1.1, are used with the difference that in this case $W_{\mu\nu}^{(m\times n)}$ is calculated from the clover average of four planar $m \times n$ Wilson loops in the μ, ν plane. The improved field strength tensor can then be written as

$$
\begin{aligned}
F_{\mu\nu(\text{IMP})} &= k_1 F_{\mu\nu}(L^{(1,1)}) + k_2 F_{\mu\nu}((2,2)) + k_3 F_{\mu\nu}(L^{(1,2)}) \\
&\quad k_4 F_{\mu\nu}(L^{(1,3)}) + k_5 F_{\mu\nu}(L^{(3,3)}),
\end{aligned}
\tag{2.7}
$$

where $k_1, \cdots, k_5$ are the improvement factors which were found by Bilson-Thompson, *et al.* [31, 32] to take the values

$$
\begin{aligned}
k_1 &= 19/9 - 55k_5 \\
k_2 &= 1/36 - 16k_5 \\
k_3 &= 64k_5 - 32/45 \\
k_4 &= 1/15 - 6k_5
\end{aligned}
$$

and k_5 being a free parameter which can be used to create 3-, 4- and 5-loop improved definitions of the field strength tensor. Again, as these are all versions of the 5-loop improvement, all definitions are $\mathcal{O}(a^4)$ improved and differ only in higher order error terms.

In their work Bilson-Thompson, *et al.* [31, 32] find that the most accurate results are obtained using the full 5-loop improved definition of the field-strength tensor with $k_5 = 1/180$, which is between the 3-loop choice of $k_5 = 1/90$ and the 4-loop choice of $k_5 = 0$. However, the results obtained with the 3-loop definition are only slightly different from the 5-loop results, but calculations using the 3-loop $F_{\mu\nu}$ are considerably cheaper than calculations using the 5-loop version. The 3-loop definition produces integer topological charge on approximately self-dual configurations to better than 4 parts in 10^4. This makes the 3-loop improved definition of the field-strength tensor

$$
F_{\mu\nu} = \frac{-i}{8}\left[\left(\frac{3}{2}W^{1\times 1} - \frac{3}{20u_0^4}W^{2\times 2} + \frac{1}{90u_0^8}W^{3\times 3}\right) - \text{h.c.}\right]_{\text{Traceless}}, \tag{2.8}
$$

which is made traceless by subtracting $1/3$ of the trace from each diagonal element of the 3×3 colour matrix, the choice for most of the calculations performed for this work.

2.2   Simulation parameters

The studies reported in this work are carried out on four different lattice sizes. Namely being $8^3 \times 16$, $12^3 \times 24$, 16^4 and $16^3 \times 32$ lattices. For evaluating the low-lying eigenmode problem the $8^3 \times 16$, 16^4 and $16^3 \times 32$ lattices were used, with the 16^4 just being used for the single instanton background. $12^3 \times 24$ and $16^3 \times 32$ lattices were used with Monte Carlo generated background fields in the vortex analysis. In both cases the smaller lattices were used to get some rough ideas and to verify the algorithms. Production runs were done on $16^3 \times 32$ lattices. Parameters for the lattices are found in table 2.1, with $\sqrt{\sigma} = 440$ MeV being used to set the values for a_σ.

These configurations are generated in a Monte-Carlo method with a plaquette plus rectangle improved action with mean-field improved coefficients. Further details of the action are found in sec. 2.1.1. I like to thank the CSSM lattice collaboration, especially D. B. Leinweber and A. G. Williams, for kindly providing these improved configurations.

β	Volume	N_{configs}	$a\sqrt{\sigma}$	a_σ [fm]	ρ_{lat}	ρ_{phys}
4.10	$12^3 \times 24$	15	0.611(20)	0.272(9)	0.1414(4)	0.379(25)
4.38	$16^3 \times 32$	100	0.368(5)	0.165(3)	0.0539(2)	0.398(30)
4.53	$16^3 \times 32$	100	0.299(11)	0.134(5)	0.0339(2)	0.380(28)
4.60	$16^3 \times 32$	100	0.272(11)	0.122(5)	0.0281(2)	0.380(31)
4.60	$12^3 \times 24$	15	0.272(11)	0.122(5)	0.0289(5)	0.391(32)
4.80	$16^3 \times 32$	100	0.207(5)	0.093(2)	0.0173(2)	0.404(20)

Table 2.1: Simulation parameters β, volumes, string tension $a\sqrt{\sigma}$, lattice spacings a and vortex densities. The values for the lattice spacings for the $16^3 \times 32$ lattices have been obtained by using 50 configurations each. For the small $\beta = 4.60$ lattice estimates are taken from the larger lattice.

2.3   Low-lying eigenmodes techniques

2.3.1   Hermitian Wilson-Dirac operator

I am going to examine localisations of eigenmodes and correlations to topological objects at the kernel level of the overlap formalism. Let me first define the hermitian operator used in the kernel.

$$H(m_0) = \gamma_5 D_{\mathrm{W}}(-m_0), \tag{2.9}$$

is the hermitian Wilson-Dirac operator with $D_{\mathrm{W}}(-m_0)$ being the Wilson-Dirac operator defined in the standard way

$$
\begin{aligned}
[D_{\mathrm{W}}(\kappa)\psi](x) \;=\;& \psi(x) - \kappa \sum_\mu [(1 - \gamma_\mu)U_\mu(x)\psi(x+\mu) \\
& + (1 + \gamma_\mu)U_\mu^\dagger(x-\mu)\psi(x-\mu)],
\end{aligned}
\tag{2.10}
$$

where the hopping parameter κ is related to the bare mass by

$$
\kappa = (8 - 2m_0)^{-1}.
\tag{2.11}
$$

The calculations are done for bare quark masses $0 \leq \mathrm{m}_0 \leq 2$, which is equivalent to $0.125 \leq \kappa \leq 0.25$ at tree level. Thus I examine eigenmodes in and just outside the region $m_c < m_0 < 2$, where m_c is the "critical-mass" which is 0 at tree-level but for non-trivial gauge fields shifts away from 0. This is the range of the mass parameter m_0 corresponding to the physical region in the overlap formalism. Modes of $H(m_0)$ crossing zero in this region are accompanied by the abrupt appearance of exact zero modes of the overlap-Dirac operator at the corresponding m_0 value [34].

2.3.2   Instanton Model

As one would like to quantify sizes and correlations of localised eigenmodes and topological objects I fit an instanton model to the obtained data. For this instanton model one needs to distinguish between a model for action or charge densities and a model for the zero-mode density [35],

$$
p(x)_{\mathrm{act}} = c \cdot \frac{6}{\pi^2} \cdot \frac{\rho^4}{((x-x_0)^2 + \rho^2)^4},
\tag{2.12}
$$

$$
p(x)_{\mathrm{zero}} = c \cdot \frac{2}{\pi^2} \cdot \frac{\rho^2}{((x-x_0)^2 + \rho^2)^3},
\tag{2.13}
$$

where x is the distance from the instanton peak at x_0 to the calculated densities. The normalisation factor c allows to fit to the instanton shape and prevents the fit from being dominated by the maximal value of the fitted object which is affected by periodic images due to the finite volume of the 4-torus. Both models are continuum results derived from the standard 't Hooft ansatz. Eq. (2.12) is the action density and is used to fit action and charge densities. Eq. (2.13) is the density of the fermion field in the zero-mode and is used to fit eigenmode densities. As I will describe in the results section this fit works very well, even if one cannot be sure, whether the objects found are really instantons. Nevertheless the model is useful for quantifying sizes and positions of the relevant objects.

2.3.3 Smooth Instanton background

In this section I will describe how a smooth instanton background is created. Such a smooth instanton background will later be used to test correlations between eigenmodes and topological objects. In this case the topological object will be the created instanton. A single instanton background on a lattice is created by performing the path integration of

$$A_\mu(x) = \frac{x^2}{x^2 + \rho^2} \left(\frac{i}{g} \right) (\partial_\mu S) S^{-1}, \tag{2.14}$$

with

$$S = \frac{x_4 \pm i \overrightarrow{x} \cdot \overrightarrow{\sigma}}{\sqrt{x^2}}, \tag{2.15}$$

where $+$ is an instanton and $-$ an anti-instanton, to create the link variable. One finds in the regular gauge

$$U_\mu^{\mathrm{reg}}(x) = \exp\left[i a_\mu(x) \cdot \sigma \phi_\mu(x; \rho) \right], \tag{2.16}$$

$$\phi_\mu(x; \rho) = \frac{1}{\sqrt{\rho^2 + \sum_{\nu \neq \mu}(x_\nu - \overline{x}_\nu)^2}} \tan^{-1} \frac{\sqrt{\rho^2 + \sum_{\nu \neq \mu}(x_\nu - \overline{x}_\nu)^2}}{\rho^2 + \sum_\nu (x_\nu - \overline{x}_\nu)^2 + (x_\nu - \overline{x}_\nu)}, \tag{2.17}$$

$$
\begin{aligned}
a_1(x) &= (-x_4 + \overline{x}_4, x_3 - \overline{x}_3, -x_2 + \overline{x}_2), \\
a_2(x) &= (-x_3 + \overline{x}_3, -x_4 + \overline{x}_4, x_1 - \overline{x}_1), \\
a_3(x) &= (x_2 - \overline{x}_2, -x_1 + \overline{x}_1, -x_4 + \overline{x}_4), \\
a_4(x) &= (x_1 - \overline{x}_1, x_2 - \overline{x}_2, x_3 - \overline{x}_3).
\end{aligned} \tag{2.18}
$$

In the singular gauge one finds[1]

$$U_\mu^{\mathrm{sing}}(x) = \exp\left[i b_\mu(x) \cdot \sigma \big(\phi_\mu(x; 0) - \phi_\mu(x; \rho) \big) \right], \tag{2.19}$$

$$
\begin{aligned}
b_1(x) &= (x_4 - \overline{x}_4, x_3 - \overline{x}_3, -x_2 + \overline{x}_2), \\
b_2(x) &= (-x_3 + \overline{x}_3, x_4 - \overline{x}_4, x_1 - \overline{x}_1), \\
b_3(x) &= (x_2 - \overline{x}_2, -x_1 + \overline{x}_1, x_4 - \overline{x}_4), \\
b_4(x) &= (-x_1 + \overline{x}_1, -x_2 + \overline{x}_2, -x_3 + \overline{x}_3).
\end{aligned} \tag{2.20}
$$

The singular gauge instanton is clearly recognisable on the volume rendered action density plot as seen in fig. 3.1 (a), which is described more closely in sec. 3.1. The outer surface shown is half the peak height.

---

[1]Note that the analogous result of [10] inverts the roles of instantons and anti-instantons

2.4   Revealing the vortex texture

To reveal if center vortex degrees of freedom are relevant for confinement one needs to look at configurations $\{Z_\mu(x)\}$, $Z_\mu(x) \in Z_N$ which are closest to, and as such represent best, the full link configurations $\{U_\mu(x)\}$, $U_\mu(x) \in SU(N)$. Z_N being the center of the group SU(N), i.e.

$$Z_\mu(x) = \exp\left(i\frac{2\pi}{N}m\right), \qquad -\frac{N}{2} < m \le \frac{N}{2}, \qquad m \in \mathbb{Z}. \qquad (2.21)$$

The maximal overlap of a center configuration with the corresponding full configuration is achieved by minimising the functional

$$\sum_{x,\mu} \left[U_\mu^\Omega(x) - Z_\mu(x)\right]^\dagger \left[U_\mu^\Omega(x) - Z_\mu(x)\right] \xrightarrow{\Omega, Z_\mu} \min, \qquad (2.22)$$

with

$$U_\mu^\Omega(x) = \Omega(x)U_\mu(x)\Omega^\dagger(x + \mu) \qquad (2.23)$$

being gauge transformed links. Minimising the functional (2.22) directly implies the maximisation of the overlap

$$R_{\text{ideal}} = \frac{1}{N_l} \sum_{x,\mu} \text{Re} \frac{1}{N} \text{Tr}\left(U_\mu^\Omega(x) Z_\mu^\dagger(x)\right), \qquad (2.24)$$

with N_l being the number of links of the lattice. It is $|R| \le 1$, with $R = 1$ implying that the full configuration can be entirely expressed in terms of center elements Z_μ after being gauge transformed. One directly sees that a suitable gauge needs to be chosen in order to achieve the maximal overlap. For this purpose several gauges have been proposed in the literature.

Most of the recent works [36, 22, 37, 17, 23, 38, 18] used a center gauge fixing method followed by center-projection. Although there were other approaches, as Abelian gauge fixing [24] and a method without gauge fixing [39], the use of the center gauge approach is most promising. There are different center gauges one can use:

- Laplacian center gauge (LCG) [23, 21]

- Indirect maximal center gauge (IMCG) [20]

- Maximal center gauge (MCG) [36, 22, 23]

with a review of all methods found in [25]. All these methods have advantages and disadvantages with MCG being the most established gauge. In the next section I will take a closer look at the MCG for SU(N) lattice gauge theory and will then specify this for SU(3).

2.4.1   Maximal Center Gauge

Unfortunately the determination of Z_μ and Ω directly from the overlap condition (eq. 2.24) is a non-trivial task. Although it is, in principle, possible to use a "simulated annealing" algorithm, the actual calculation of Z_μ and Ω to the needed precision is very costly and therefore beyond the scope of this work. But I will come back to the ideal gauge condition R_{ideal} (eq. 2.24) using an iteration overrelaxation algorithm and a previously MCG gauge-fixed configuration in sec. 4.5. If one agrees to choose one of the suboptimal gauges already proposed in the literature and mentioned in the previous subsection, the calculation will be feasible. The most established gauge being MCG, for which the gauge condition formally follows from eq. 2.24 with the assumption that $\frac{1}{N}\mathrm{Tr}U_\mu^\Omega(x)$ comes close to a center element. This assumption leads to two gauge conditions [22, 23] called "*baryonic*" and "*mesonic*":

$$R_{\mathrm{bar}} \;=\; \frac{1}{N_{site}N_{dim}N^N} \sum_{n,\mu} \mathrm{Re}\left([\mathrm{Tr}U_\mu(n)]^N\right), \qquad (2.25)$$

$$R_{\mathrm{mes}} \;=\; \frac{1}{N_{site}N_{dim}N^2} \sum_{n,\mu} |\mathrm{Tr}U_\mu(n)|^2, \qquad (2.26)$$

where N_{site} is the number of lattice sites and N_{dim} the number of dimensions. R satisfies $|R| \leq 1$ for both equations. The use of the mesonic gauge condition (eq. 2.26) allows for a Cabibbo-Marinari [40] inspired method of maximizing R. This method for SU(N) was derived from a SU(2) method [26] by Montero [36]. It is interesting to note that maximising R via eq. 2.26 is equivalent to maximising the trace in the adjoint representation which is not affected by center gauge transformations. It is not clear whether the "*mesonic*" gauge condition (eq. 2.26) really yield the larger overlap in eq. 2.24, or if the "*baryonic*" gauge condition (eq. 2.25), or even a combination of both, would be best. This problem and some resulting difficulties will be addressed in the "results" section in more detail.

One has to locally find the gauge transformation Ω for each lattice site which maximises the local quantity

$$R_x = \sum_\mu |\mathrm{Tr}\{\Omega(x)U_\mu(x)\}|^2 + |\mathrm{Tr}\{U_\mu(x-\mu)\Omega^\dagger(x)\}|^2. \qquad (2.27)$$

Instead of trying to find the optimal SU(N) gauge transformation at once, Ω is obtained from a SU(2) matrix $g = g_4\mathbb{1} - i\vec{g}\vec{\tau}$ which is then included into one of the $N(N-1)/2$ SU(2) subgroups of SU(N). With this R_x can be written as

$$R_x = \sum_{i,j=1}^4 \left(\frac{1}{2}g_i a_{ij} g_j\right) - \sum_{i=1}^4 g_i b_i + c, \qquad (2.28)$$

with a_{ij} being a real symmetric $4{\times}4$ matrix, b_i a real 4-vector and c a real constant, all of which are depending on the link variables $U_\mu(x)$ and $U_\mu(x-\mu)$. The SU(2) matrix g, which maximises R_n in eq. 2.28 can be found using standard numerical algorithms, see sec. 2.4.1 below.

Once g is found, the SU(N) matrix Ω is known and all links U_μ attached to the site x are updated. The procedure needs to be repeated for all $N(N-1)/2$ SU(2) subgroups of SU(N) and for all lattice sites. Covering the whole lattice once with this procedure is called one center gauge fixing sweep. The gauge fixing procedure can stop, if R is stable within a given precision.

To clarify the algorithm, I'm going to go into more details for SU(3) in the next subsection.

Technical details for SU(3)

In the case of SU(3) gauge theory, the transformation matrix is $\Omega \in \mathrm{SU}(3)$. There are three SU(2) subgroups one can embed into SU(3). I choose to do it as follows:

$$\Omega_1 = \begin{pmatrix} g_1 & 0 \\ 0 & 1 \end{pmatrix}, \tag{2.29}$$

$$\Omega_2 = \begin{pmatrix} 1 & 0 \\ 0 & g_2 \end{pmatrix}, \tag{2.30}$$

$$\Omega_3 = \begin{pmatrix} g_{3_{11}} & 0 & g_{3_{12}} \\ 0 & 1 & 0 \\ g_{3_{21}} & 0 & g_{3_{22}} \end{pmatrix}, \tag{2.31}$$

with $g_{1,2,3} \in \mathrm{SU}(2)$. For SU(2) matrices the relations $g = g_0 \mathbb{1} + i\vec{g}\vec{\tau}$, with $\vec{\tau}$ being the Pauli-matrices, and $g_0^2 + \vec{g}^2 = 1$ hold.

The goal is to maximise

$$R = \sum_\mu \left(|\mathrm{Tr}\{\Omega(x)U_\mu(x)\}|^2 + |\mathrm{Tr}\{U_\mu(x-\mu)\Omega^\dagger(x)\}|^2 \right) \tag{2.32}$$

$$= \sum_\mu \left(|\mathrm{Tr}\{\Omega(x)U_\mu(x)\}|^2 + |\mathrm{Tr}^*\{\Omega(x)U_\mu^\dagger(x-\mu)\}|^2 \right), \tag{2.33}$$

by finding the local gauge transformation $\Omega(x)$ which achieves this.

In order to maximise R in eq. 2.33 one needs to find the corresponding SU(2) matrix g which maximises

$$\mathrm{Tr}\left\{ \begin{pmatrix} g & 0 \\ 0 & 1 \end{pmatrix} \underbrace{\begin{pmatrix} M & b \\ c^T & a \end{pmatrix}}_{U_\mu} \right\} = \mathrm{Tr}_2(g \cdot M) + a, \tag{2.34}$$

with M being the sum of two unitary 2×2 matrices, $M = m_1 + im_2$, with $m_{1/2} = a_0 \mathbb{1} + i\vec{a}\vec{\tau}$ and $a = a_\mathrm{R} + ia_\mathrm{I}$, which are given from the corresponding link $U_\mu(x)$. Using this decomposition one can write

$$
\begin{aligned}
|\mathrm{Tr}\{\Omega(x)U_\mu(x)\}|^2 &= |\mathrm{Tr}_2(g \cdot m_1) + a_\mathrm{R} + i\mathrm{Tr}_2(g \cdot m_2) + ia_\mathrm{I}|^2 \\
&= (\mathrm{Tr}_2(g \cdot m_1) + a_\mathrm{R})^2 + (\mathrm{Tr}_2(g \cdot m_2) + a_\mathrm{I})^2, \quad (2.35)
\end{aligned}
$$

which is for practical reasons best written in a matrix and vector format

$$
|\mathrm{Tr}\{\Omega(x)U_\mu(x)\}|^2 = \begin{pmatrix} g_0 \\ \vec{g} \end{pmatrix}^T A \begin{pmatrix} g_0 \\ \vec{g} \end{pmatrix} + \begin{pmatrix} g_0 \\ \vec{g} \end{pmatrix} \vec{b} + \underbrace{a_\mathrm{R}^2 + a_\mathrm{I}^2}_{c}, \quad (2.36)
$$

with A being a 4×4 matrix and $\vec{b}$ being a 4-vector both containing the sum over μ, as well as $U_\mu(x)$ and $U_\mu^\dagger(x-\mu)$. Finding the maximum of R can be done via the Lagrange multiplier method with the constraint $g_0^2 + \vec{g}^2 - 1 = 0$. For this method it is best to change into the eigenvector base of A. Finding the eigenvectors and eigenvalues can be done via standard numerical algorithms, e.g. Jacobi. This leads to

$$
R = \sum_k \frac{b_k^2}{4}\left(\frac{\lambda_k}{(\lambda_k - \lambda)^2} - \frac{2}{(\lambda_k - \lambda)} \right) + c, \quad (2.37)
$$

and

$$
\sum_k \frac{b_k^2}{4(\lambda_k - \lambda)^2} = 1, \quad (2.38)
$$

with λ_k being the eigenvalues of A, b_k being the components of $\vec{b}$ and λ being the Lagrange multiplier. It is easy to find R_max with the constraint of eq. 2.38. Then g can be determined via

$$
\vec{g} = -\frac{\vec{b}}{2(\lambda_k - \lambda)}, \quad (2.39)
$$

and a transformation to the original base.

Once $\Omega(x)$ is found, the links touching the site x are updated via

$$
\begin{aligned}
U_\mu^\Omega(x) &= \Omega(x)U_\mu(x)\Omega^\dagger(x+\mu), & (2.40) \\
U_\mu^\Omega(x-\mu) &= \Omega(x-\mu)U_\mu(x-\mu)\Omega^\dagger(x), & (2.41)
\end{aligned}
$$

where $\Omega(x-\mu) = \Omega^\dagger(x+\mu) = \mathbb{1}$. This whole procedure is repeated for all three SU(2) subgroups and the SU(3) gauge transformations $\Omega(x)$ are constructed as in eqs. 2.29, 2.30 and 2.31. After the updates for all SU(2) subgroups are done one can move to the next lattice point. Covering the whole lattice in this manner is called a center gauge fixing sweep.

To get stable values for R within a precision of 10^{-6} takes roughly 1100 sweeps for configurations on a lattice with the size of $16^3 \times 32$.

2.4.2 Center Projection

In this section the process of identifying vortices with the help of a center projection mechanism is discussed. Once the center vortices are identified the vortex density and other values of interest can be calculated.

The center projection replaces a link $U_\mu(x)$ with a center element $Z_\mu(x)$ of the gauge group SU(N), which is closest to the $U_\mu(x)$ of the full configuration,

$$U_\mu(x) \rightarrow Z_\mu(x) \tag{2.42}$$

where

$$Z_\mu(x) = \exp\left(i\frac{2\pi}{N}m\right), \qquad -\frac{N}{2} < m \leq \frac{N}{2}, \qquad m \in \mathbb{Z}. \tag{2.43}$$

Note that to find the closest center element to the full configuration one has to take the gauge transformation Ω into account, as well, as described in sec. 2.4. The maximal center gauge transformation, see sec. 2.4, or any other gauge transformation used in this work, will be considered *ideal* for this purpose at the time of use. Although it might be revealed that some other gauge fixing procedures are *ideal*. Therefore the center projection will be done on the gaugefixed links $U_\mu^\Omega(x)$. To maximise the overlap between $U_\mu^\Omega(x)$ and $Z_\mu(x)$ one needs to minimise the functional

$$\sum_{x,\mu} \left[U_\mu^\Omega(x) - Z_\mu(x)\right]^\dagger \left[U_\mu^\Omega(x) - Z_\mu(x)\right] \xrightarrow{\Omega, Z_\mu} \min \tag{2.44}$$

As mentioned above, the gauge is chosen, therefore the minimisation with respect to the center elements can be performed locally. Calculate

$$\frac{1}{N}\mathrm{Tr}U_\mu^\Omega(x) = u_l \exp\left(i\varphi^l\right), \tag{2.45}$$

for each link, then the closest center element

$$Z_\mu(x) = \exp\left(i\varphi_m^l\right), \tag{2.46}$$

with

$$\varphi_m = \frac{2\pi}{N}m, \tag{2.47}$$

is the one where

$$\varphi^l - \varphi_m^l \rightarrow \min. \tag{2.48}$$

The theory based upon configurations created with center projection will be called "vortex-only", throughout this work.

2.4.3   Vortex identification

In order to extract physics, which is influenced by center vortices, one first needs to identify the center vortices on the lattice. After having performed a center projection as described above this is easily done. One needs to calculate the plaquette

$$v(p) := \prod_{x,\mu} Z_\mu(x) = \exp\left(i\frac{2\pi}{N}\phi\right), \tag{2.49}$$

where $\phi = \sum_{x,\mu} m(x,\mu)$, being the sum over the values for m of the center elements belonging to the plaquette p. In case of SU(3) one says a vortex with center charge

$$z = \exp\left(i\frac{2\pi}{N}\phi\right), \tag{2.50}$$

pierces the plaquette if

$$\phi \mod_3 = -1, 1. \tag{2.51}$$

One says that no vortex pierces the plaquette if

$$\phi \mod_3 = 0. \tag{2.52}$$

2.4.4   Vortex removal

After having identified vortices one is able to create a second configuration similar to the one where the vortices where identified, but with all the vortices removed. Creating such a configuration and doing calculations, e.g. the static quark-antiquark potential, with it, reveals which physical properties are actually influenced by vortices.
To remove the vortices one simply needs to replace all links $U_\mu(x)$ with links $U'_\mu(x)$ given by

$$U'_\mu(x) = Z^\dagger_\mu(x) \cdot U_\mu(x), \tag{2.53}$$

where $Z^\dagger_\mu(x)$ is the hermitian conjugate of the center element $Z_\mu(x)$ calculated as in sec. 2.4.2. In the following, "vortex-removed" will denote the theory based upon configurations created with this procedure.

2.5   The static quark-antiquark potential

The static quark-antiquark potential is probably the easiest and best way to test confining properties of a theory. A linearly rising potential for large distances shows that the underlying theory is confining. If there is only a Coulomb part and the potential is flat for large distances the theory is non-confining. Calculations of the quark-antiquark potential are fairly straightforward, nevertheless some points need to be considered.

Several methods for performing and enhancing such calculations have been proposed during the last 20 years. The method used in this work for calculating the potential consists of ideas by Stack [41] and the enhancement method proposed by Bali and Schilling [42, 43]. I will describe the method more closely in the following two subsections.

2.5.1   Ground state overlap enhancement

In lattice gauge theory interesting physical quantities like masses, matrix elements and potential values, in which we are interested here, are related to asymptotic properties of exponentially decreasing correlation functions in Euclidean time. This poses some difficulty in separating physical values from the noise. One is forced to improve the operator to reach the desired asymptotic behaviour for a small T region. The so-called overlap enhancement procedure has proven to be a valuable tool to achieve this.

The relation between Wilson loops $W(R,T)$ and the ground state potential $V(R)$ is given by

$$W(R,T) = C(R) \exp\left\{-TV(R)\right\} \ + \ \text{excited state contributions.} \quad (2.54)$$

To increase the contribution from the first term, one needs to enhance the ground state overlap $C(R)$ for each value of R. In principle this is done by cooling the spatial links only, replacing $U_i(x) \to \Pi_i(x)$, where

$$\Pi_i(x) = \mathcal{P}_N \sum_{k=\pm 1,\ldots,3\neq i} U_k(x)U_i(x+k)U_k^\dagger(x+i), \qquad i=1,2,3, \quad (2.55)$$

with $\mathcal{P}_N$ being the projector onto the "closest" SU(N) element. For SU(2) the effect of the operator $\mathcal{P}_2$ is given by

$$\mathcal{P}_2 M = \frac{1}{\sqrt{a_0^2 + \vec{a}^2}}\left(a_0 + i\vec{\tau}\vec{a}\right), \quad (2.56)$$

M being an SU(2) matrix given by $M = a_0 + i\vec{\tau}\vec{a}$ with the Pauli Matrices τ^a. Temporal links are not being touched by this procedure, i.e.,

$$\Pi_0(x) = U_0(x). \quad (2.57)$$

In the case of SU(3), however, the projection $\mathcal{P}_3$ is computationally expensive. For further details on the $\mathcal{P}_3$ projection operator see [43]. An interesting and effective way to reduce the computer time needed is a Cabbibo-Marinari inspired method recently proposed by Langfeld [23].

Let me define the action of the spatial links of a given time slice t by

$$S_{(3)}(t) = \sum_{i>k,1\ldots3} P_{ik}(x),\qquad\qquad(2.58)$$

with $P_{ik}(x)$ being the plaquette calculated from the spatial links. In addition, one needs to consider embeddings of the SU(2) matrix $M = a_0 + i\vec{\tau}\vec{a}$, with $a_0^2 + \vec{a}^2 = 1$, into SU(3). For details see sec. 2.4.1, i.e. eqs. 2.29, 2.30, 2.31, further up. The "cooling procedure" now consist of a loop over the three SU(2) subgroups for each spatial link $U_l(x)$. In more detail: $U_l(x)$ is substituted by $U' = \Omega_1 U_l(x)$, then the action $S_{(3)}$ is locally maximized with respect to Ω_1. Subsequently U' is replaced by $U'' = \Omega_2 U'$ and the action is maximized with respect to Ω_2. The third step is setting $U''' = \Omega_3 U''$ and maximizing $S_{(3)}$ with respect to Ω_3. The "cooled" link is then defined as

$$\Pi_l(x) = \Omega_3 \Omega_2 \Omega_1 U_l(x).\qquad\qquad(2.59)$$

One sweep repeats this procedure for every spatial link on the lattice. The maximization of the action $S_{(3)}$ with respect to one of the SU(2) subgroups can be implemented very efficiently, thus this procedure can be considered computationally cheap. This whole procedure is gauge covariant.

To enhance the ground state overlap, the above procedure is applied recursively. The Wilson loop expectation value $\langle W(R,T)\rangle$ is then calculated from the ensemble $\{\Pi_\mu(x)\}$ and not from the original Monte-Carlo generated configuration $\{U_\mu(x)\}$. In agreement with Langfeld [23] I find that ten sweeps of this procedure are enough to yield more than 0.99 ground state overlap.

2.5.2   The potential

The relation between the Wilson loop and the potential is given by eq. 2.54. For $T \gg R$ one gets for the Wilson loop expectation value

$$\langle W(R,T)\rangle \to \exp\left[-TV(R)\right],\qquad T \gg R.\qquad\qquad(2.60)$$

With the overlap enhancement this relation holds for smaller values of T, i.e., Langfeld [23] finds a linear behavior in T for $-\ln\langle W(R,T)\rangle$ for $T \geq 3$. For different values of R one can fit a function linear in T to $-\ln\langle W(R,T)\rangle$,

$$-\ln\langle W(R,T)\rangle = \gamma T + \delta.\qquad\qquad(2.61)$$

The coefficients γ can be interpreted as the potential in lattice units $V(Ra)a$. This quantity is shown in the potential plots in sec. 4.4. The line shown in these plots is a fit according to the function

$$V(r)a = cR - \frac{b}{R} + V_0, \qquad r = Ra. \tag{2.62}$$

The parameter c can be interpreted as $c = \sigma a^2$, which is the string tension in units of the lattice spacing. This method is inspired by Stack [41] and was recently used by e.g. Stack *et al.* [24].

Chapter 3

The hermitian Wilson Dirac operator and topology

This chapter is dedicated to the results found for the first main part of this work. Correlations between low-lying eigenmodes and topological objects, which could be instantons, are examined. Qualitative results an visualisation of eigenmode- and topological charge densities are presented in the following two sections. The qualitative results are then quantified in sec. 3.3. Results from this chapter have been published in [13].

3.1   Smooth Instanton background

In this section I will present the results for a smooth instanton background field created as described in sec. 2.3.3. Calculations for this section were performed on $8^3 \times 16$ and 16^4 lattices. As mentioned in sec. 2.3.3 the artifically created singular gauge instanton is clearly recognizable on the volume rendered action density plot as seen in fig. 3.1 (a). The outer surface shown is half the peak height.

The results seen on the smaller exploratory lattice are also found on the 16^4 lattice. The instanton on the latter lattice is cooled for two sweeps to minimise boundary effects. Eigenmodes of this configuration are calculated for $0.12 \leq \kappa \leq 0.27$ with an increment of 0.01 between values. The first four eigenvalues of the spectrum are shown in fig. 3.2, followed by an evaluation of the localisation of $\rho(x)$ for the first three low-lying eigenmodes for each κ. This is done by plotting $\rho(x)$ as seen in fig. 3.1 for selected eigenmodes.

For eigenmodes with $\kappa \ll \kappa_{\mathrm{c}} = 0.125$ a rather uniform distribution of $\rho(x)$ is found whereas eigenmodes for all κ, $\kappa_{\mathrm{c}} < \kappa < 0.27$ are strongly localised. For the lowest eigenmode this localisation strongly corresponds to the localisation of the instanton in the action density plot as seen by comparing fig. 3.1 (a) and fig. 3.1 (b), (c). One therefore finds that the eigenmode displays strong correlation
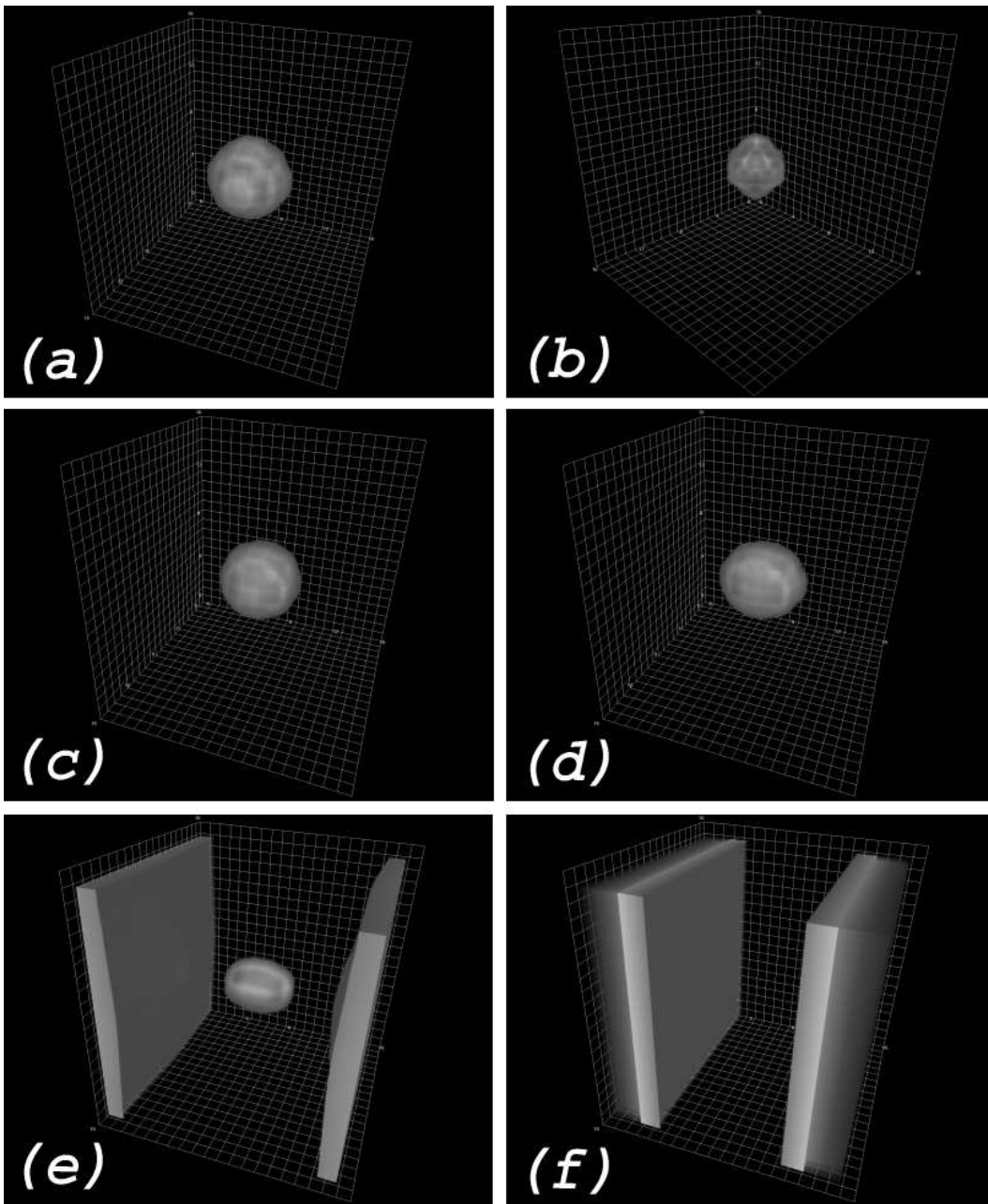
39

Figure 3.1: (a) Action density of a single instanton configuration on a 16^4 lattice. (b) First eigenmode for the single instanton configuration for $\kappa = 0.19$. Note the very strong correlation with the instanton on the action density. (c) First eigenmode for the single instanton configuration for $\kappa = 0.25$. Again note the strong correlation between the eigenmode and the action density. (d) Second eigenmode for the single instanton configuration for $\kappa = 0.25$. The localisation has a prolate shape compared to the spherical instanton. (e) Second eigenmode for the single instanton configuration for $\kappa = 0.19$. The localisation has a wall like shape with a prolate correlation to the instanton. (f) Third eigenmode for the single instanton configuration for $\kappa = 0.19$. The eigenmode has a wall like shape and is not correlated with the instanton. For all figures a volume rendering of the corresponding density is shown. The outer isosurface is half the peak density.
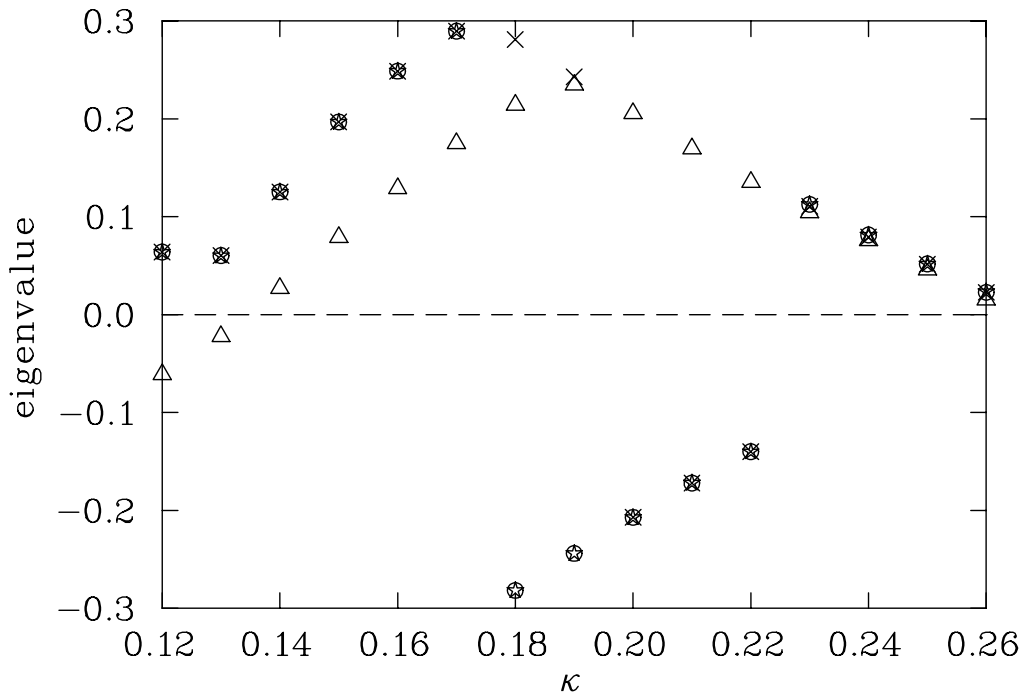
Figure 3.2: Smallest four eigenvalues of the eigenvalue spectrum of a smooth single instanton configuration on a 2-sweep cooled 16^4 lattice. For the open triangles there is strong spherical correlation between the eigenmode and action density and behaviour as described in the text. For the other symbols there is correlation with prolate-like shapes and wall-like structures. The shapes are shown in fig. 3.1. For $\kappa = 0.20, 0.21$ and 0.22 the fifth eigenvalue is expected to lie degenerate with the open triangles.

with the instanton. The size and shape of this correlation varies from broad with some wall like structures for $\kappa \leq \kappa_c$ to very small for $\kappa_c < \kappa < 0.19$ and is getting broader again for larger values of κ. For higher eigenmodes this localisation gets broader and less correlated with the instanton. Some higher eigenmodes show no correlation with the instanton but just wall like structure as seen in fig. 3.1 (f). Others show prolate-like correlations as seen in fig. 3.1 (d). Some eigenmodes also show a wall-like structure and a prolate-like correlation as seen in fig. 3.1 (e). It is useful to note that plane wave behaviour would display uniform behaviour in the density plot.

3.2 Monte-Carlo-generated SU(3) gauge field background

In the last section I showed that the low-lying eigenmodes of the Wilson-Dirac operator are strongly correlated to the instanton on a single-instanton configuration. As a next step one might be interested if this is also true on standard Monte-Carlo generated SU(3) background fields. I will show in this section that the idea indeed holds for Monte-Carlo generated background fields. To do this I investigate three hot and three cooled configurations on both $8^3 \times 16$ ($\beta = 4.38$) and $16^3 \times 32$ ($\beta = 4.60$) lattices. Three-loop improved cooling [31, 32, 44, 30], as mentioned in sec. 2.1.2, is used to cool the configurations for 12 sweeps. This is just enough to get clear structure in the action and topological charge. As a reference for comparison of the eigenmode density the action and topological charge density of the cooled configuration is used. This is done because those densities are too rough for the hot configuration and no accurate comparison would be possible. As there is more structure observed on the topological charge density plot, I use this as a preferred reference. See fig. 3.4 (a) for a typical topological charge density plot of a $16^3 \times 32$ configuration. However, the action density plot is also useful for guidance.

One can say an eigenmode is correlated to a topological object if $\rho(x)$ has a peak within one lattice site of the peak topological charge density. The first four eigenmodes for values of $0.13 \leq \kappa \leq 0.25$ for cooled configurations and $0.15 \leq \kappa \leq 0.29$ for hot configurations in steps of 0.01 are calculated. This range is from approximately 0.02 smaller than κ_c to a region where doublers appear in the overlap formalism. I find that the behaviour described in the following is general for all configurations: Each of the eigenmodes is localised. This was already observed for the lowest eigenmode [12]. For $\kappa < \kappa_c$ this localisation weakens and the density, $\rho(x)$, broadens quickly. An exponential decay of the density $\rho(x)$, as previously observed [12], seems likely to occur. All low-lying eigenmodes for $\kappa \geq \kappa_c$ are correlated to topological objects.

It is possible to track a correlation along the modes for all $\kappa \geq \kappa_c$ and for one step smaller than κ_c. Thus a mode can be labeled by its correlation. Fig. 3.3 shows eigenmodes of a hot configuration, where the symbol used denotes which topological object the localised low-lying eigenmode is correlated with. Careful inspection of fig. 3.3 reveals the presence of an eigenmode, correlated to one topological object, but with a spectral flow containing two zero crossings. As the point where the mode crosses zero is associated with the size of the correlated object, this suggests that the object is either a lattice artifact, or there are two objects with different sizes close together. I will take a closer look at this behaviour in the next section, where the sizes of the objects and eigenmodes are quantified.
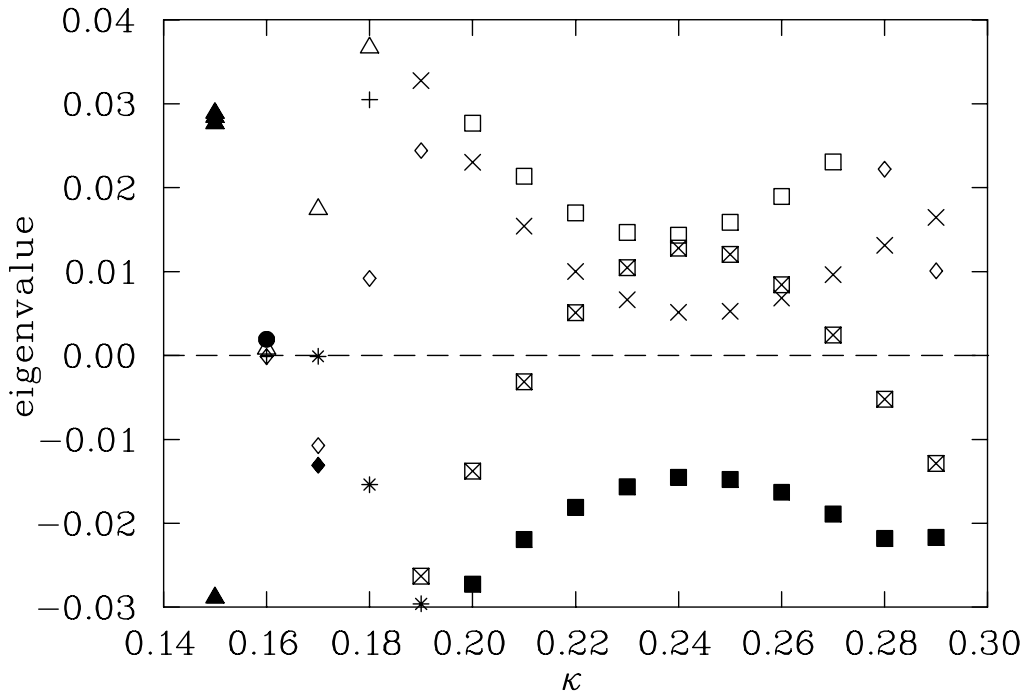
Figure 3.3: Smallest four eigenvalues of the eigenvalue spectrum of a hot configuration showing correlations of eigenmodes to topological objects. Each eigenmode has a correlation to one topological object and each different symbol indicates a different topological object. Modes for $\kappa = 0.15 < \kappa_c$ are very broad and weakly correlated to several objects.

Around κ_c and towards the upper end of the analysed spectrum, localisations are weak. However, the correlation of positions is strong. At these κ there is a tendency to get correlations to more than one topological object. The localisations get stronger and sharper for increasing values of κ until a maximal localisation is reached for a value κ, which will be defined to be κ_{max}. For $\kappa > \kappa_{max}$ the localisations get weaker again. Fig. 3.4 shows a visualisation of this behaviour. Additional colour figures can be found on the web [45]. A closer look at this behaviour will be taken in the next section.

For the lower eigenmodes, which are separated by a gap from the higher eigenmodes, one finds correlation to one topological object per eigenmode. For higher eigenmodes , which are closer together with some degenerate modes, one finds correlations to more than one topological object. In general it can be said that the closer the eigenvalues and the weaker the actual localisations, the more likely it is to get correlation with more than one topological object in the corresponding
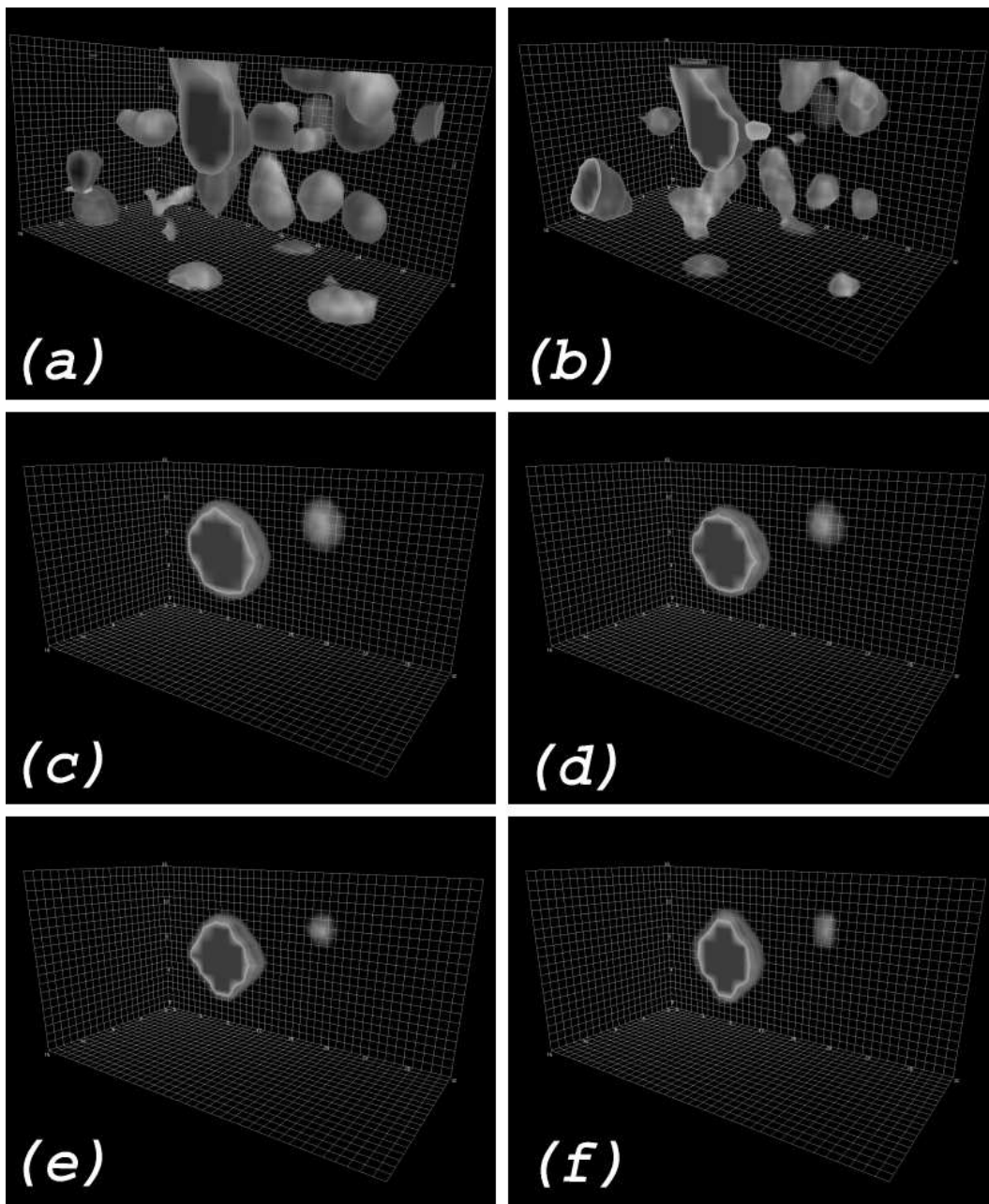
Figure 3.4: (a) Topological charge density of a 12-sweep cooled $16^3 \times 32$ configuration at $\beta = 4.60$. (b) Action density of the same configuration. There is clearly less structure for the action density than the topological charge density. (c) The low-lying eigenmode density at $\kappa = 0.14$ of the same, but uncooled, configuration with correlation to the object seen in the action density and the topological charge density. (d) Eigenmode density at $\kappa = 0.16$ showing correlation to the same topological object. (e) Eigenmode density at $\kappa = 0.18$. The localisation is maximal for this value of κ. (f) Eigenmode density at $\kappa = 0.19$. The localisation gets broader again.

eigenmodes.

Calculations of 20 eigenmodes for selected values of κ on hot configurations show only little broadening in the localisations and persistent correlations with topology. This suggests that this behaviour will not change quickly and such correlations will persist for even higher eigenmodes.

As mentioned above, the topological charge density of the 12-sweep cooled configuration is used for comparison. The position of eigenmodes on cooled fields agree perfectly well with the position of topological objects seen in this density. A typical distance between such positions being 0.05 lattice spacings a. For hot configurations some of the correlations are slightly offset compared to the structure in the smoothed configurations whereas other structure in the eigenmodes has no corresponding structure in the smoothed topological charge. But in those cases a comparison with a less cooled configuration reveals correlations between eigenmodes and topological objects which are moved or destroyed by further cooling. This behaviour is expected and understood: Topological objects are known to move under cooling as instantons and anti-instantons attract each other and annihilate when they are close enough together.

This clear correlation between $\rho(x)$ of eigenmodes on hot configurations and topological objects suggests that it is possible to identify areas through the noise of a hot configuration with significant topology. This allows to "see through" the noise by using eigenmodes of the hermitian Wilson-Dirac operator.

The spectral plot of the first four eigenvalues of a 12-sweep cooled configuration looks different compared to the same plot on a hot configuration. Comparing fig. 3.3 and fig. 3.5 one notices the rhomboid shape with an area without any eigenvalues in the spectral plot of the cooled configuration. This is expected for such smoothed configurations [46, 47]. Eigenmodes on the right-hand side of this rhomboid behave different than eigenmodes on the left-hand side of the rhomboid. The localisation of the eigenmodes on the left-hand side is approximately the same as the localisations in the hot configuration. But the eigenmodes on the right-hand side are much weaker in localisation. Those weaker localised eigenmodes are related to very high eigenmodes in the hot configuration and the process of cooling brings them into an area where they can be observed as low eigenmodes. These eigenmodes must be very high eigenmodes in a hot configuration for they are much weaker localised as localisations seen for up to the 20th eigenmode in a hot configuration. Although the behaviour in localisation strength for eigenmodes of cooled configurations is different from that of eigenmodes of hot configurations the correlations with topological objects still exist for all eigenmodes. I will take a

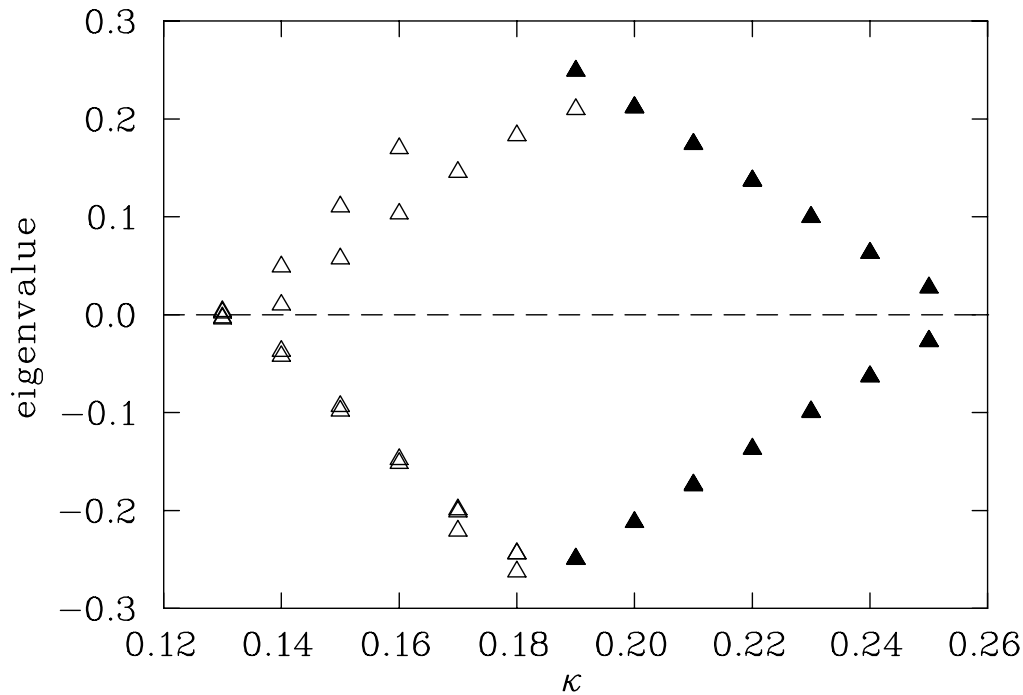closer look at localisation strength and quantify it in the next section.

Figure 3.5: First four eigenvalues of the spectrum of a 12-sweep cooled configuration. Note the rhomboid shape with the area without eigenvalues. The modes to the right of the maximum, the filled symbols, are only weakly localised. The open symbols are strongly localised.

3.3 Quantitative Results

As described above, the localisation of the eigenmodes change shape and size with changing of κ. In order to quantify this behaviour I found two useful methods. The first one is fairly simple. I have already showed that most eigenmodes are localised at one topological object. As the eigenmodes are all normalized, the maximum, or peak, value of the eigenmode density is an indicator of how strong this localisation is. Fig. 3.6 shows the plot of such peak values for four eigenmodes each of three hot $16^3 \times 32$ configurations. This plot shows a smooth behaviour with a maximum for $\kappa_{\mathrm{max}} \approx 0.23$ for the lowest eigenmodes. This suggests that for hot SU(3) configurations the strongest localisation occurs in that κ region.

Fig. 3.7 shows the same plot for four eigenmode densities each for three 12-sweep cooled $16^3 \times 32$ configurations. This plot shows a different behaviour. Again there
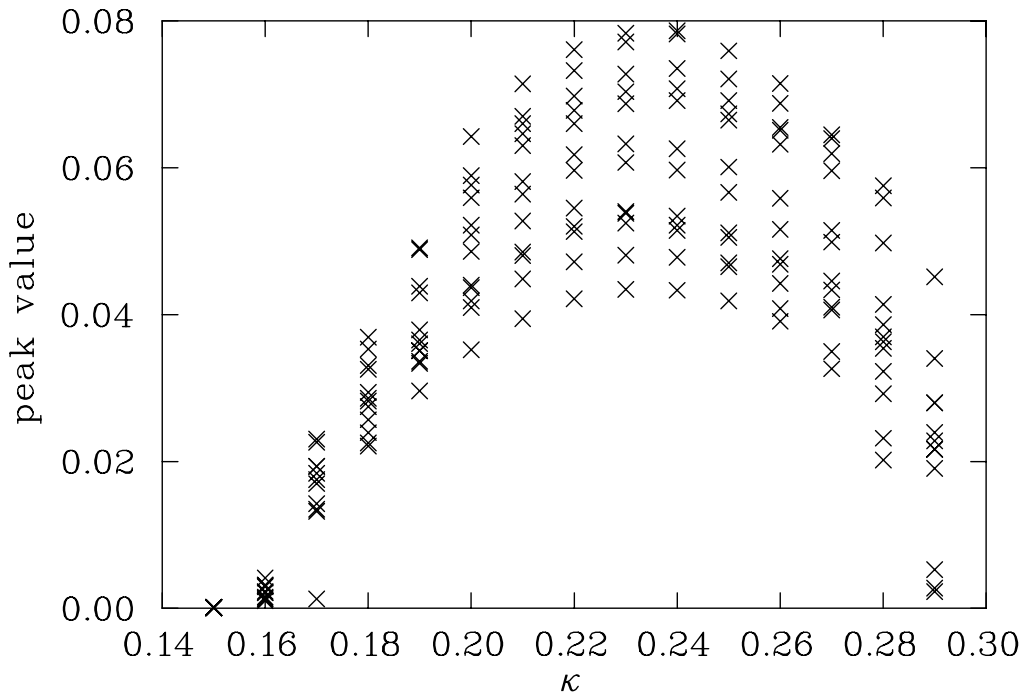
Figure 3.6: Peak value of four eigenmode densities each from hot $16^3 \times 32$ configurations with respect to κ

is a clear peak, but the values drop to almost zero immediately after the peak. However, after the qualitative observations presented in the previous section, this was expected. These low maximum values correspond to weakly localised modes, which are on the right-hand side of the spectrum shown in fig. 3.5. In this case κ_{max} can not be determined, for it is not clear how the localisations are going to develop if the the stronger localised eigenmodes would be followed up to higher values of κ. The one eigenmode that could be followed suggests that $\kappa_{\mathrm{max}} \approx 0.20$. This reduction of κ_{max} is about the same size as the reduction of κ_{c} for going from the hot to the 12-sweep cooled configuration.

To get more information about the shape of the eigenmodes, the instanton model, eq. 2.14, is fitted to the eigenmodes. This model gives very good fits as

$$\sum_x (p(x)_{\mathrm{zero}} - p_{\mathrm{M}}(x))^2 = 10^{-5} \tag{3.1}$$

where $p_{\mathrm{M}}(x)$ is the 6 parameter fit of 3^4 points of $p(x)$ centered about the peak of $\rho(x)$. This value is about 1000 times smaller than the peak value and 10^{-5} is the worst case with most of the fits of order 10^{-7} to 10^{-9}. The fit parameter ρ is then a good measurement for the size of the localisation.
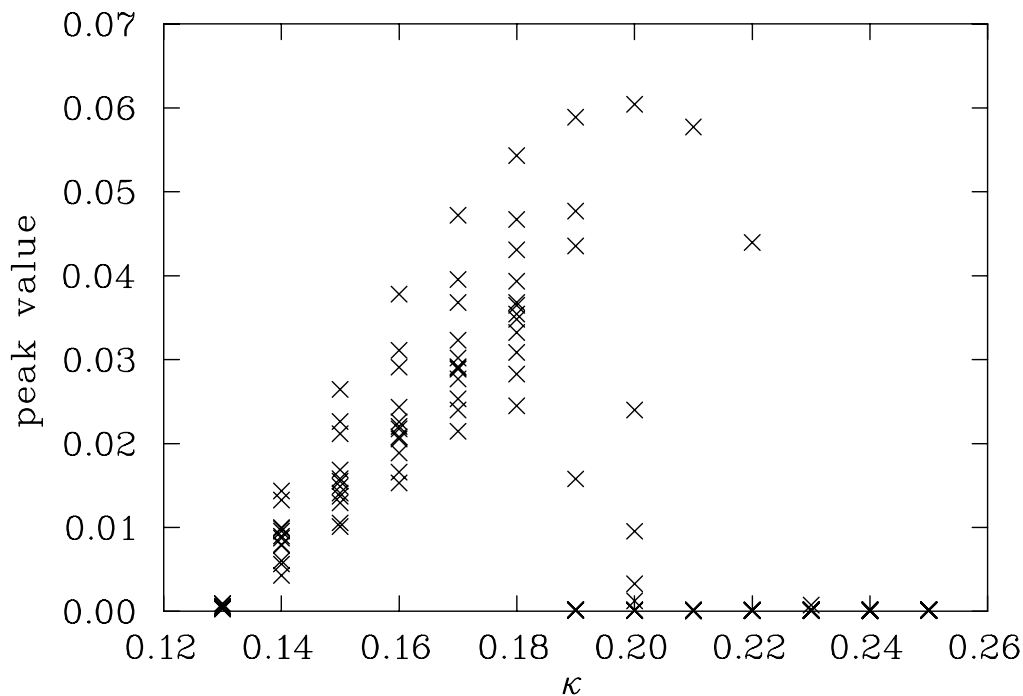
Figure 3.7: Peak value of four eigenmode densities each from three 12-sweep cooled $16^3 \times 32$ configurations with respect to κ

In fig. 3.8 $\rho(\kappa)$ is plotted for four eigenmodes calculated on all hot configurations and in fig. 3.9 for four eigenmodes calculated on all 12-sweep cooled configurations. One sees a behaviour which corresponds to the behaviour described above for the peak values of the eigenmodes. For the hot configurations $\rho(\kappa)$ shows a smooth behaviour with a minimum around $\kappa_{\mathrm{max}} = 0.26$. This means the eigenmodes are maximally localised for this value of κ and are less localised for both ends of the spectrum. The κ_{max} found this way varies slightly from κ_{max} found by just taking the peak values of the eigenmode densities. It is about 0.03 larger at 0.26 for the lowest eigenmode. As mentioned earlier the eigenmodes for low and high values of κ are localised on more than one topological object. Therefore fig. 3.8 reports more local maxima than modes at these κ. However in the range $0.18 \leq \kappa \leq 0.28$ only one local maximum is found per mode.

In the previous sections it has been established that low-lying eigenmodes are correlated to a single topological object when eigenmodes are non degenerate. It is also established that an instanton gives rise to a zero crossing in the spectral flow with the sign of the slope equal to the sign of the topological charge [10]. However, as mentioned above, fig. 3.3 reveals an eigenmode correlated to one
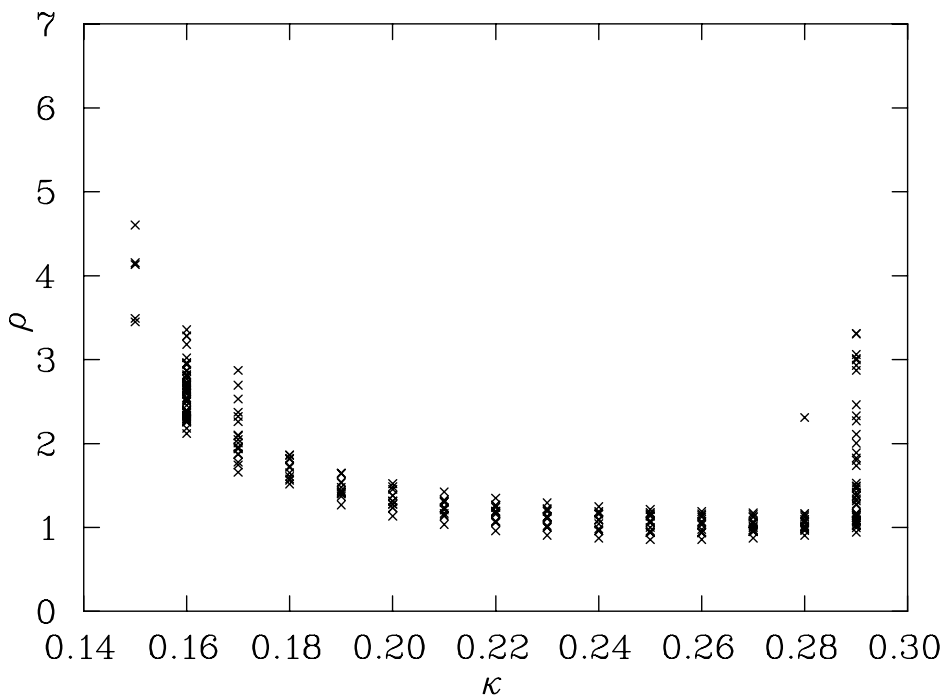
Figure 3.8: ρ of the fitted instanton model of four eigenmodes from three hot $16^3 \times 32$ configurations with respect to κ. Note that there are several correlations in one eigenmode at both ends of the spectrum.

topological object, but with two zero crossings. The size of the eigenmode varies from $\rho = 1.2$ to $\rho = 1.0$ as κ varies from 0.21 to 0.27. The size of the correlated object on the topological charge density, which can only be seen on the 5-sweep-cooled configuration, is $\rho = 1.1$. It is possible to reproduce similar spectral flows on single instanton configurations, which have been cooled with the Wilson action to the point where the topological charge is $Q \approx 0.4$, well below 1. Hence the double zero crossing of the spectral flow in fig. 3.3 either suggests the presence of a lattice artifact or the presence of small topological objects on top of the larger observed one. This issue is still work in progress, as it is also interesting how an improved fermion action acts on such a double-crossing. Some preliminary results have been reported [48] with some others being currently prepared [49]. This current work suggest that improved actions, such as FLIC, see sec. 2.1.1, do not remove the double crossings, but rather tend to keep them. An interpretation for this behaviour is that such double-crossings are a manifestation of short range topological fluctuations, which are still "seen" by a "good" improved action, but removed by a crude improved action, such as a Wilson action where all links are smeared.
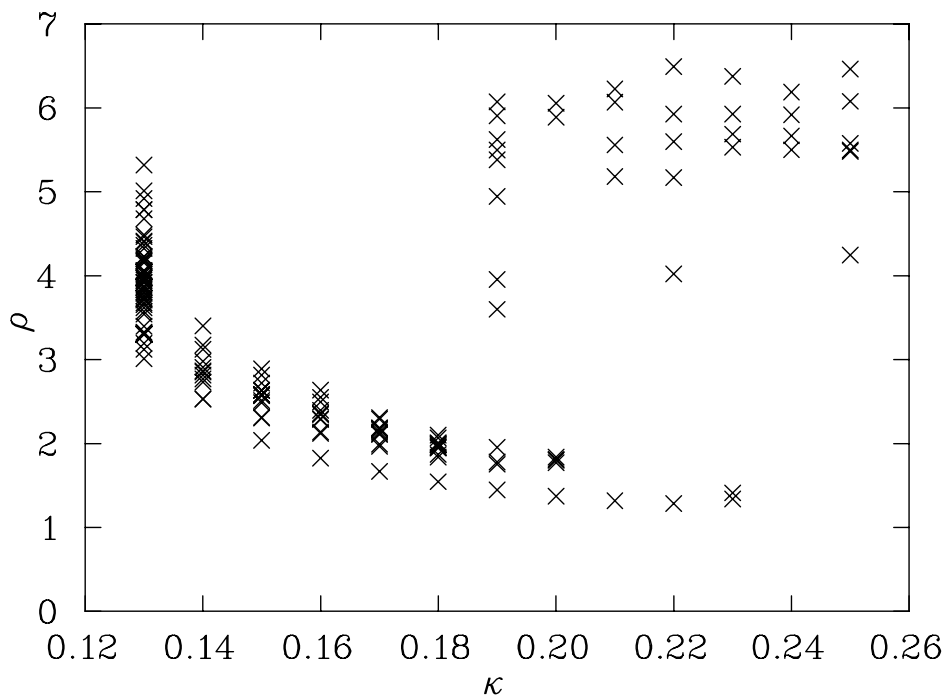
Figure 3.9: ρ of the fitted instanton model of four eigenmodes from three 12-sweep cooled $16^3 \times 32$ configurations with respect to κ. Note the jump at $\kappa \approx 0.19$.

The behaviour of $\rho(\kappa)$ of the cooled configurations shows a jump at $\kappa \approx 0.19$, where the weakly localised modes set in as described above. Some of these weakly localised modes are not sufficiently localised to allow a fit to the instanton model. A fit would result in values for $\rho \geq 10$, which are not reasonable for the instanton model and therefore neglected. Where a fit to those eigenmodes is possible, it results in large values of ρ compared to the strongly localised eigenmodes. One finds that ρ is about 2 for strongly localised eigenmodes and about 6 for weakly localised eigenmodes. For $\kappa \leq 0.19$, $\rho(\kappa)$ decreases smoothly, but for $\kappa \geq 0.19$ the values of $\rho(\kappa)$ are higher than at the lower end of the spectrum and do not show a smooth behaviour. Again it is hard to extract κ_{max}, but it seems that if the stronger localised modes could be followed further it would be around 0.22. This is about 0.02 larger than the κ_{max}, which is extracted using the peak values.

The fitting of the models to the eigenmode densities, using eq. 2.13, as well as to the topological charge densities, using eq. 2.12, allows comparison of the sizes for the eigenmode localisations with the sizes of the actual topological objects. In order to do this, the topological object which is located closest to the position of the eigenmode is found. However the instanton model can only be fitted to topological charge densities of cooled configurations, as only those are smooth enough.

Therefore only the sizes of eigenmodes of cooled configurations can be compared with sizes of actual topological objects. Due to the different localisation strength for eigenmodes on the left-hand and on the right-hand side of the rhomboid spectrum of a cooled configuration, those eigenmodes are considered separately.
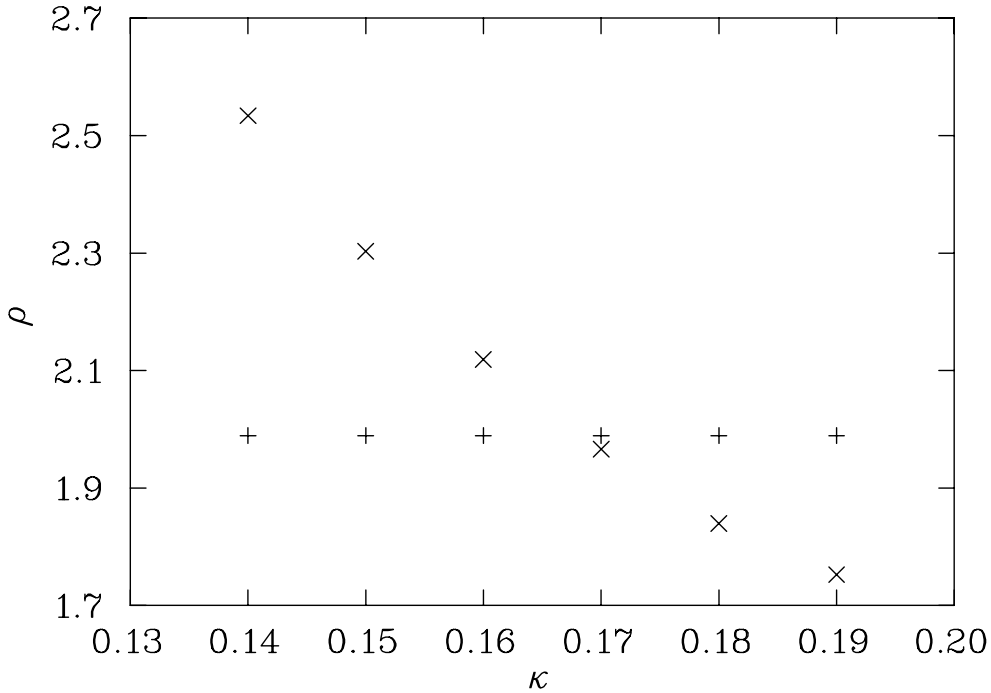

Figure 3.10: ρ of the fitted instanton model of one mode of a 12-sweep cooled $16^3 \times 32$ configuration with respect to κ. The $\times$ denote the size of the eigenmode and the $+$ denote the size of the correlated topological object. That the two graphs cross is a general result and all crossings are found for $0.155 < \kappa < 0.175$.

The fitted positions for the strongly localised eigenmodes agree very well with the fitted positions of the correlated topological objects lying within a fifth of a lattice spacing, and most of the times even better. The fitted positions of the weakly localised modes to the right-hand side of the spectrum agree only within one lattice spacing with their correlated topological objects. Strongly localised eigenmodes are correlated to smaller objects in the topological density. Such eigenmodes on the left-hand side of the eigenvalue spectrum, except those for $\kappa \leq \kappa_{\mathrm{c}}$, have a size between $\rho \approx 1.5$ and $\rho \approx 3.5$. The correlated topological objects have a size between $\rho \approx 2$ and $\rho \approx 3$. The eigenmodes are larger than their correlated topological objects for smaller values of κ, but as they shrink with growing κ they get smaller than their correlated topological objects. All followed modes reach the size of the correlated topological object for $0.155 < \kappa < 0.175$. Fig. 3.10 shows

an example of this behaviour.

The weakly localised eigenmodes on the right-hand side of the eigenvalue spectrum are larger than the strongly localised eigenmodes on the left-hand side of the spectrum. They turn out to have a size between $\rho \approx 4$ and $\rho \approx 6$. But the topological charge density objects correlated with those eigenmodes are themselves bigger than the topological charge density objects correlated with the stronger localised modes. The sizes of the topological charge density objects lie between $\rho \approx 3$ and $\rho \approx 4$. The weaker localised eigenmodes are always bigger than the correlated topological objects with $\rho_{\mathrm{mode}} \approx \rho_{\mathrm{topQ}} + 2$. For $\kappa = \kappa_{\mathrm{c}}$ the size of the eigenmodes is between $\rho = 3$ and 5 with a relation to the size of the correlated topological objects of $\rho_{\mathrm{mode}} \approx \rho_{\mathrm{topQ}} + 1$. Sizes of strongly localised eigenmodes of hot configurations are of a comparable, but slightly smaller size than the ones on cooled configurations.
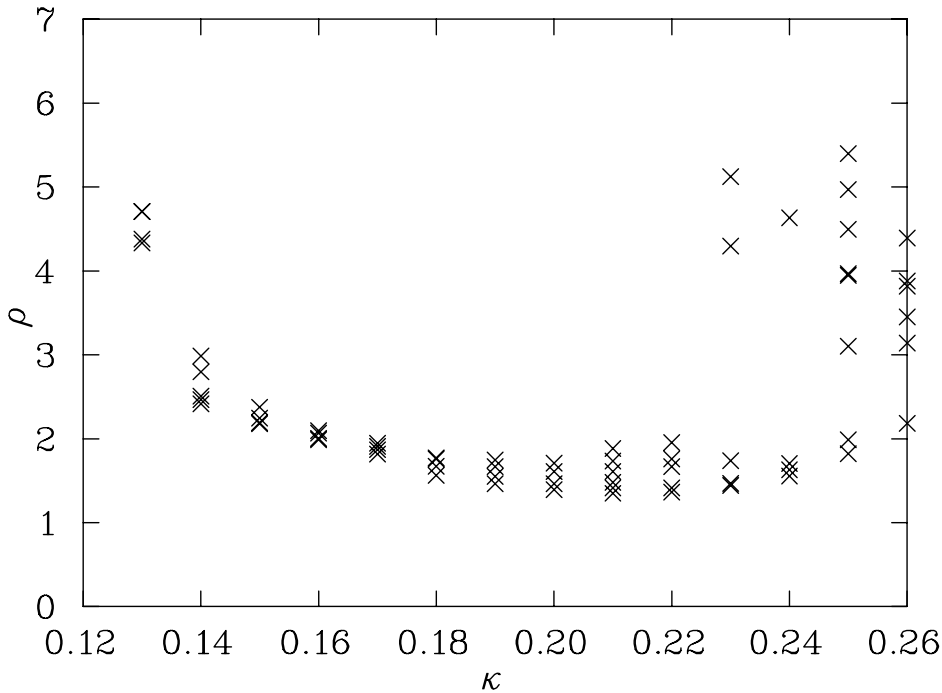

Figure 3.11: ρ of the fitted instanton model of four eigenmodes for one 4-sweep cooled $16^3 \times 32$ configuration with respect to κ. Note the jump occurring at higher κ compared to fig. 3.9.

In order to understand why modes on the right-hand side of the rhomboid are just weakly localised spectra for one configuration with different amounts of cooling are calculated. This shows that the value of κ where the jump in the localisation size

occurs becomes smaller with cooling. Compare fig. 3.9 and fig. 3.11. It is known [10] that zero crossings for larger κ correspond to smaller topological objects. As the localisation sizes of calculated eigenmodes shrink with growing κ as well, one can generally think of larger values of κ being associated with smaller objects. Cooling removes smaller objects first, therefore eigenmodes for large κ become "unassociated" with small objects. The eigenmodes show a behaviour of weak localisation which can be seen in fig. 3.9 and fig. 3.11 after the jump. Further cooling removes larger objects and therefore the value of κ, where the change of behaviour sets in, becomes smaller.

Chapter 4

The vortex picture of confinement

In this chapter I will present the results from the vortex part of this work. Calculations for this chapter were performed on $8^3 \times 16$, $12^3 \times 24$ and $16^3 \times 32$ lattices. For more informations about the simulation parameters see sec. 2.2 and table 2.1 therein. The smaller lattices were just used for checking the algorithms and getting rough ideas. Production was done on 16×32 lattices with four different values of β, namely $\beta = 4.38$, 4.53, 4.60 and 4.80, with 100 configurations each.

In the following sections I will describe the steps needed to establish a vortex picture of confinement and the results obtained in these steps.

4.1 Wilson-loop phases

Before gauge fixing and identifying center degrees of freedom let me first present some new evidence that such degrees of freedom indeed play an important role for calculations connected to Wilson-loops.

Calculations of n × n Wilson-loops $W(x)$ with full Monte-Carlo generated SU(3) lattice configurations show that the complex phases ϕ given by $W(x) = e^{i\phi}$ are not uniformly distributed. Instead the probability for having a certain ϕ is strongly peaked at three values. These are

$$\phi_m = \frac{2\pi}{3}m, \qquad m = -1, 0, 1, \tag{4.1}$$

which corresponds to the three center elements of SU(3). Fig. 4.1 shows histograms with the total number of Wilson loops having a phase ϕ plotted over ϕ for different sizes of Wilson-loops. Counts for a 0.001 rad interval are summed. For n = 1 only the peak at $m = 0$ is present, but with increasing n this peak decreases and two more peaks begin to form at $m = -1$ and $m = 1$. For n = 4, which corresponds to a physical size of the Wilson-loop of $0.488\,\mathrm{fm} \times 0.488\,\mathrm{fm}$ for the $\beta = 4.60$ lattice shown in the plot, the peaks reach (almost) equal height.

Even larger Wilson-loops do not change the situation any further. This behaviour is quantified in fig. 4.2, where the relative peak height of the $-2\pi/3$ peak is plotted. The relative peak height is determined by the counts for loops having a phase ϕ with $-\pi/3 \leq \phi < \pi/3$ divided by the counts for loops having a phase ϕ with $-\pi \leq \phi < -\pi/3$. Although the relative peak height is not purely dependent on the size of the Wilson-loop, but also on the lattice spacing a one finds that for large enough Wilson-loops this ratio goes to one.

The result that large Wilson-loops are dominated by center degrees of freedom is the same as Langfeld finds in his analysis of vortex limited Wilson-loops for SU(3) [23]. The analysis in [23], however, takes information from Z_3 configurations found after gauge fixing to MCG into account. This might put some kind of bias into the analysis. Contrary to that, the analysis presented here is performed on full SU(3) configurations and only the number of Wilson-loops having a certain phase ϕ is plotted. Thus this approach is gauge invariant and there is no bias put into this analysis, at all. Therfore this finding is strong evidence that the center plays an important role for Wilson-loops, which makes center vortices a prime ansatz for work on the confinement problem. Note that this finding, of course, agrees with the Wilson loop expectation values being real. The average of the complex phases is zero.

4.2 MCG gauge fixing

To correctly determine physical center vortices the Monte-Carlo generated lattice configurations need to be gauge fixed. For reasons described in sec. 2.4 the maximal center gauge (MCG), see sec. 2.4.1 for details, is chosen as the "main" gauge for this work. "Main" meaning that most of the work will be done with MCG, but to highlight some difficulties and possible solutions two other gauges, the ideal center gauge (ICG) and the Laplacian center gauge (LCG), will be mentioned below.
The gauge fixing is done to a precision of 10^{-6}, which is a reasonable compromise between accuracy and computational effort. The value of R, as defined in eq. 2.32, stays stable within that precision after approximately 1100 gauge fixing sweeps. The values of R reached for different lattice spacings a are shown in fig. 4.3. The closer the value found for R to one the closer the links are to center elements. It seems to be the case that for lattices with a smaller lattice spacing a the gauge fixed configurations $\{U_\mu^\Omega(x)\}$ are closer to center configurations $\{Z_\mu(x)\}$. However no conclusion about the quality of these gauge fixed configurations for the vortex picture can be drawn from that, yet.
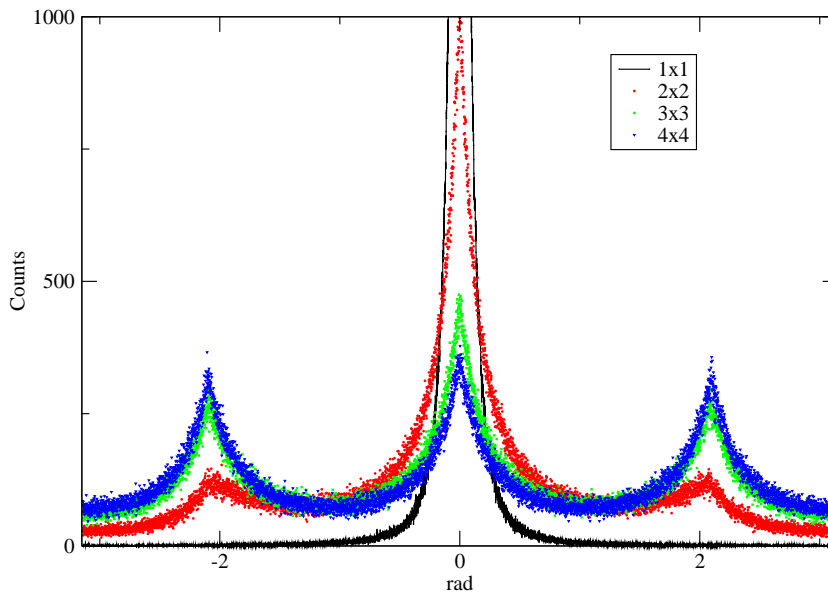
Figure 4.1: Number of Wilson-loops having the complex phase ϕ plotted over ϕ for a full $\beta = 4.60$ SU(3) configuration. For small Wilson-loops there is one strong peak for $\phi = 0$. The larger the loop, the stronger the peaks at $\phi = \pm 2\pi/3$. For $n \geq 4$ the phases are equally distributed around $\phi = \pm 2\pi/3$ and $\phi = 0$.

After the gauge fixing, vortices are identified and then removed by a projection procedure. For technical details see sec. 2.4.3 and sec. 2.4.4. The configurations with the vortices, after the MCG gauge fixing are the basis for a vortex-only theory. The vortex-removed theory is based upon the configurations created after the projection procedure.

4.3   The vortex density

After having gauge fixed to MCG, I can now identify the center vortices with the procedure described in sec. 2.4.3. The first question one is interested in is whether the vortices identified in such a way are physical. In order to show this I need the vortex density ρ defined by

$$\rho_{\text{lat}}(\beta) := \frac{\#\,\text{plaquettes pierced by a vortex}}{\#\,\text{plaquettes on the lattice}}, \tag{4.2}$$
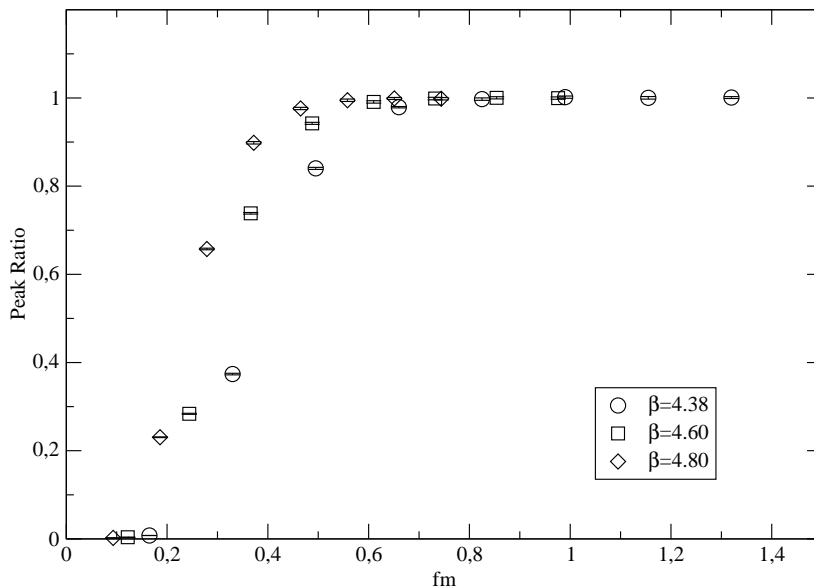
Figure 4.2: Relative peak height of the $-2\pi/3$ peak to the center peak of fig. 4.1 vs the side length n of corresponding Wilson-loops in fm. The larger the loop the closer the ratio to one.

which is equivalent to

$$\rho_{\text{lat}}(\beta) = \rho a^2(\beta) = \mathcal{P}_\beta, \tag{4.3}$$

with $\mathcal{P}_\beta$ being the probability that a plaquette carries a non-trivial center charge. If the vortex density is a physical quantity it has to be valid in the continuum limit. Thus the physical vortex density

$$\rho_{\text{phys}} = \frac{\rho_{\text{lat}}}{a^2\sigma} = \frac{\rho}{\sigma}, \tag{4.4}$$

has to be independent of the lattice spacing a.

Some evidence for asymptotic scaling can already be seen when plotting the vortex density in lattice units $\rho_{\text{lat}} = \rho a^2$ with respect to β on a logarithmic scale. This is done in fig. 4.4. The linearity of the values in this scale may be interpreted as some evidence for asymptotic scaling. The physically more interesting plot, however, is fig. 4.5. It clearly shows the independence of the lattice spacing a for the vortex density ρ_{phys} in physical units within errorbars. This is very strong evidence that the center vortex density ρ is a lattice independent quantity and as such sensible
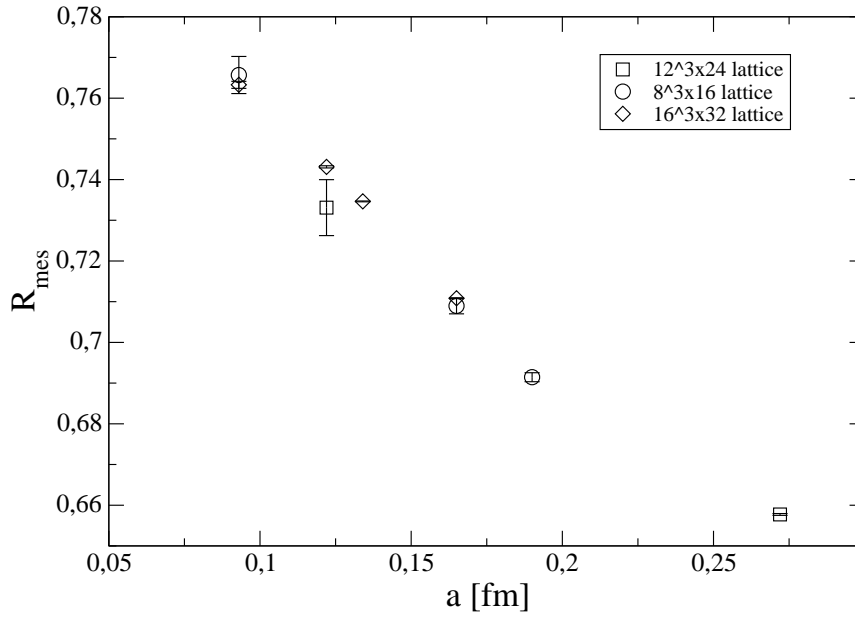
Figure 4.3: MCG gauge fixing maximization quantity R versus physical lattice spacing $a\,[\mathrm{fm}]$

in the continuum limit. One can therfore say that criterium (i) which I proposed in sec. 1.2 is fulfilled. But what about criterium (iii)? To get more insight I calculate the average physical vortex density for all lattice spacings a, which is reasonable to do as ρ_{phys} is independent of a. This yields $\rho_{\emptyset}/\sigma = 0.391(27)$ and with $\sqrt{\sigma} = 440$ MeV

$$\rho_{\emptyset} = 1.97(14)\frac{1}{\mathrm{fm}^2}. \tag{4.5}$$

This value comes close to the value $\rho_{\emptyset_{\mathrm{RV}}} = 0.5\sigma$ for the random vortex model. With this one can assume that criterium (iii) holds.
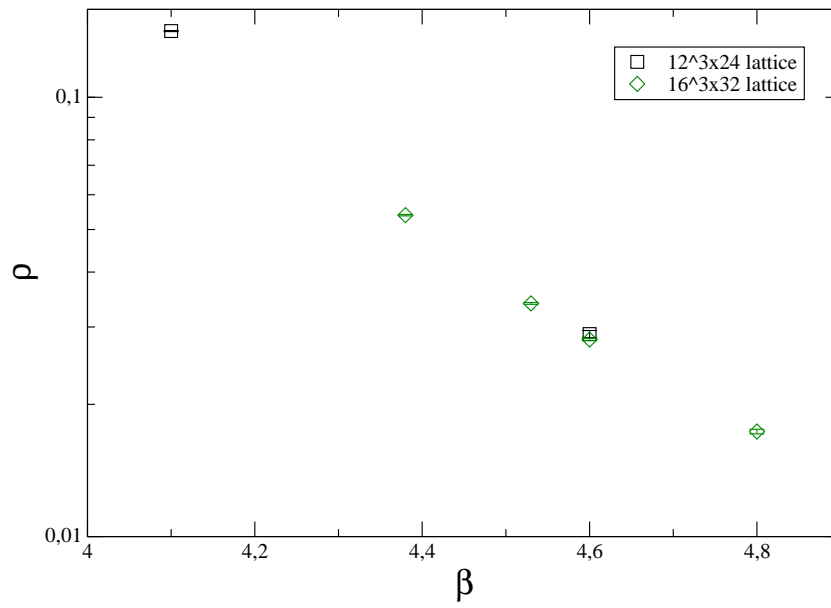
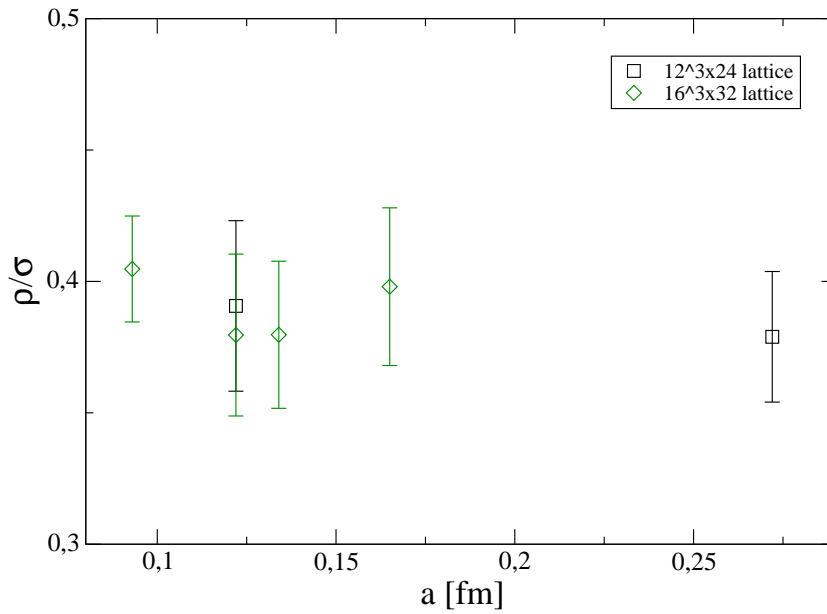Figure 4.4: Vortex density ρ in lattice units over β in logarithmic scale. Evidence for asymptotic scaling.

Figure 4.5: Vortex density ρ in physical units. Within errorbars ρ is independent of the lattice spacing a.

4.4   The potential in the MCG vortex picture

Now that vortices found after MCG gauge fixing are established as physical objects
let me take a closer look at the confining properties of the vortex theory. This
will be done by examining the static quark-antiquark potential for the full SU(3)
theory, the vortex-only theory and the vortex-removed theory. Details about the
quark-antiquark potential are to be found in sec. 2.5.
As a reference the potential of the full SU(3) gauge theory is plotted in each po-
tential plot, see figures 4.6, 4.7, 4.8 and 4.9. The black line is a fit according to
the function 2.62. The potential is the standard confining $Q\bar{Q}$-potential with a
Coulomb part for small $r\sqrt{\sigma}$ and a linearly rising part, the confining part, for large
$r\sqrt{\sigma}$.

The potential calculated in the vortex-only theory, see fig. 4.6, shows, as expected,
only the linearly rising part. Thus the vortex only theory is a confining theory.
However, in contrast to SU(2) [20, 26] and preliminary SU(3) [22] results the
vortex-only configurations reproduce only about 62% of the full string tension.
Complete string tension data for vortex-only and vortex-removed theories, as well
as, different gauges, is to be found in table 4.1. This result agrees with Langfeld
[23], who used background gauge fields created with the standard Wilson-action.
Thus the use of improved operators does not seem to change the MCG vortex
behaviour significantly. One straightforward thought is the missing string tension
might have something to do with the Gribov copy problem affecting the MCG
gauge fixing procedure. If this was the case at least some vortex configurations
should show a much larger string tension. However this is not found, thus one can
conclude that Gribov copies are not a problem for the MCG vortex picture. Ideas
of how to account for the missing 38% of the full string tension will be presented
in the following subsections.

The string tension almost vanishes for vortex-removed configurations in MCG.
The best data is obtained from the larger physical volumes, see the differences in
fig. 4.7. It is therefore desired to do the calculations on large enough lattices. For
the lattices used in this work, large enough seems to be the case for $\beta = 4.38$,
$\beta = 4.53$ and $\beta = 4.60$. For the $\beta = 4.60$, $16^3 \times 32$ lattice this corresponds roughly
to a physical volume of $(1.49\,\mathrm{fm})^3 \times 3.35\,\mathrm{fm}$. With this straightforward method it
seems that this is about the smallest volume for which one gets a non-confining
vortex-removed theory. For all physical volumes, even for the smallest one, the
remaining string tension in the vortex-removed theory is much smaller than the
missing string tension in the vortex-only theory. The straightforward conclusion
from this fact is, that the missing string tension can not be due to vortices not
found during the vortex identification process. If this was the case the remaining
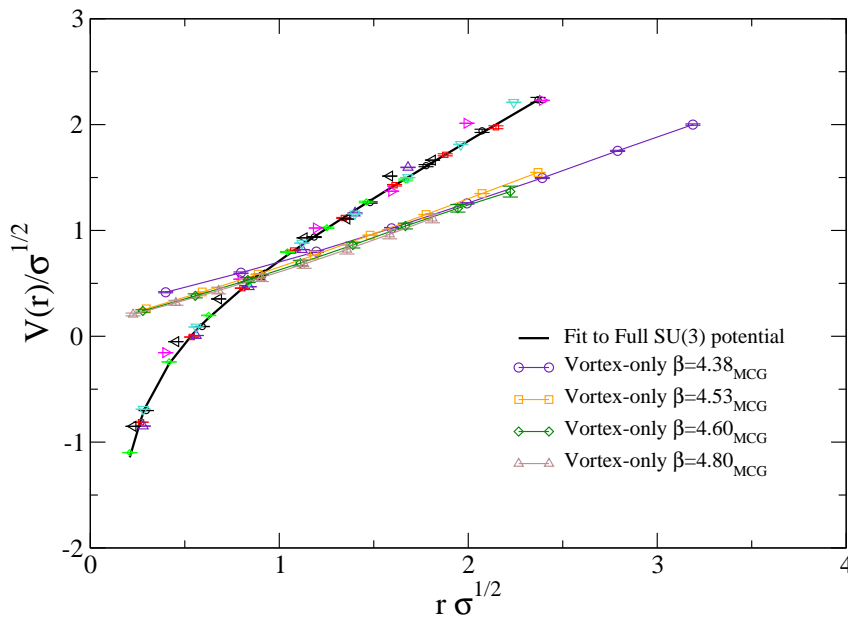
Figure 4.6: Static quark-antiquark potential for the MCG vortex-only theory and the full SU(3) gauge theory for comparison. The black line is a fit according to eq. 2.62

string tension in the vortex-removed theory would be at least of the order of the missing string tension, thus some other possibilities have to be considered, as will be done in the next sections.

4.5 Ideal center gauge

The last section showed that MCG center vortices in a vortex-only theory, reproduce only about 62% of the full string tension. It immediately comes to ones mind that this could be due to the *mesonic* gauge condition, of which one does not know if it really yields the best overlap, see sec. 2.4.1. To test if the overlap can be improved, I take the MCG gauge fixed configurations and imply the *ideal* gauge condition (eq. 2.24) via an iteration overrelaxation procedure, which maximises R_{ideal}. One sweep of this procedure consists of the following two steps at each lattice site. Firstly, get a new center element $Z_\mu(x)$ with the probability of

$$p = \exp\left[\beta_f \mathrm{ReTr} U_\mu^\Omega(x) Z_\mu^\dagger(x)\right], \tag{4.6}$$
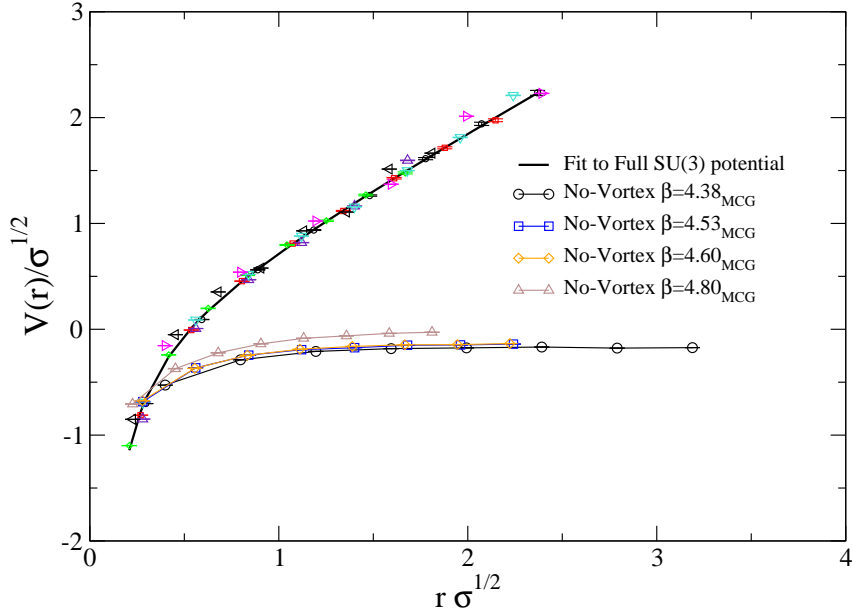
Figure 4.7: Static quark-antiquark potential for the MCG vortex-removed theory and the full SU(3) gauge theory for comparison. Note that only for $\beta \leq 4.60$ the string tension vanishes. The vanishing of the string tension depends on the physical lattice volume.

where β_f is a free parameter for the algorithm, which allows sub-optimal updates with a certain probability. After finding a new $Z_\mu(x)$ the one needs to find a gauge transformation $\Omega(x)$, which achieves

$$\mathrm{ReTr}\left(U_\mu^\Omega(x)Z_\mu^\dagger(x)\right) \to \max. \tag{4.7}$$

For getting the optimal R_{ideal}, the free parameter β_f can be tuned. My tuning procedure finds a β_f which changes R_{ideal} more than 5% from its start value. Then 20 sweeps are done with this value for β_f to leave a possible local maximum of R. After that β_f is successively increased by 0.35 every 20 sweeps. This ensures that no maximum will be missed due to large jumps for the Z_μ. In the following, the gauge produced by this procedure will be called ideal center gauge (ICG). A random start version of ICG, where one sweep of random gauge transformation is performed before the start of the ICG procedure, was tested, as well. No significant difference was seen between the random start and standard ICG gauge fixing, see the $\beta = 4.38$ potential in fig. 4.8 and fig. 4.9, thus I concentrated on the standard

ICG gauge fixing.

ICG inherits the desired properties from MCG. The vortex density is independent of
the lattice parameter β, but with a value of $\rho_\emptyset/\sigma = 0.508(31)$ it is slightly higher
than for MCG, but even closer to the random vortex model value of $\rho_{\emptyset_{\mathrm{RV}}} = 0.5\sigma$.
Again using $\sqrt{\sigma} = 440$ MeV one gets

$$\rho_\emptyset = 5.04(15)\frac{1}{\mathrm{fm}^2}. \tag{4.8}$$

These values were obtained using 20 configurations each for $\beta = 4.38, 4.60$ and
4.80. There are relatively large statistical errors in the potential plots when using
only 20 configurations, but it is still sufficient to see if there are any severe differ-
ences between the two gauges.

In order to see the differences in the confining properties between MCG and ICG the
static quark-antiquark potential for the vortex-only, fig. 4.8, and vortex-removed,
fig. 4.9, theories found after ICG gauge fixing is calculated. The string tension for
the vortex-only and vortex-removed theories are calculated, however the situation
is not changed by the ICG gauge condition. The String tension for the vortex-only
theory is only about 58% of the full string tension, thus even a few percent lower
than for MCG. This shows that the *ideal* gauge condition does not yield better
results than the *mesonic* gauge condition, but rather similar values. Thus MCG
implemented in the described way seems to be a good approximation to the ideal
case. For detailed results of the MCG/ICG vortex-only and vortex-removed string
tension in percentage of the full SU(3) string tension see table 4.1.

One big drawback of this gauge fixing method is the ambiguity in technical details
of the iteration overrelaxation algorithm. How strong should the gauge condition
be implied during the procedure? Of course one would like to have a strong gauge
fixing condition which really maximises R_{ideal}. In reality, however, it seems to be
the case that weaker the gauge condition employed the larger the string tension
reproduced by the vortex-only theory. In principle one could therefore try to de-
termine the best set of parameters for the algorithm on a trial and error basis.
However, it is not clear whether the best set of parameters necessarily yields the
full string tension in the resulting vortex-only theory. But even if this was the case,
this trial and error method yields no clean gauge condition, which could provide
more insight in the physics of the connection between center vortices and confine-
ment.

The last two sections showed that neither the *mesonic* nor the *ideal* gauge condition
yield a vortex theory which reproduces the full string tension with vortices only and
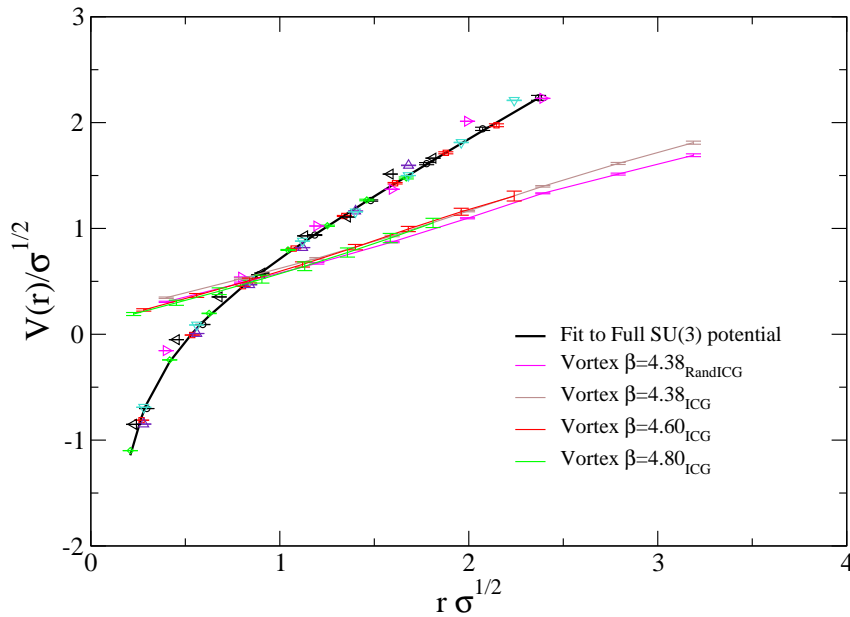
Figure 4.8: Static quark-antiquark potential for the ICG vortex-only theory. The full SU(3) gauge theory is plotted for comparison. No significant difference between MCG (fig. 4.6) and ICG potentials is seen. The random start ICG vortex-only theory has a slightly smaller string tension than standard ICG version.

no string tension without vortices. I will show two ways of dealing with this problem in the following two sections.

4.6   The missing string tension

The first way is to find a possible explanation for the missing string tension. As mentioned above the vortex-only theory reproduces only about 60% percent of the full string tension, however the vortex-removed theory has almost no string tension. This is a puzzling result as, if one tries to account the missing 40% of the string tension to some objects other than the vortices, these 40% should still be present in the vortex-removed case. The conclusion from this result is, that the missing string tension is produced by something removed with the vortices, but not present for center vortices only. An idea of incorporating this into the vortex picture has been proposed by Jeff Greensite and Stefan Olejnik [50]. The idea is to introduce an additional phase κ, which can represent the missing string tension.
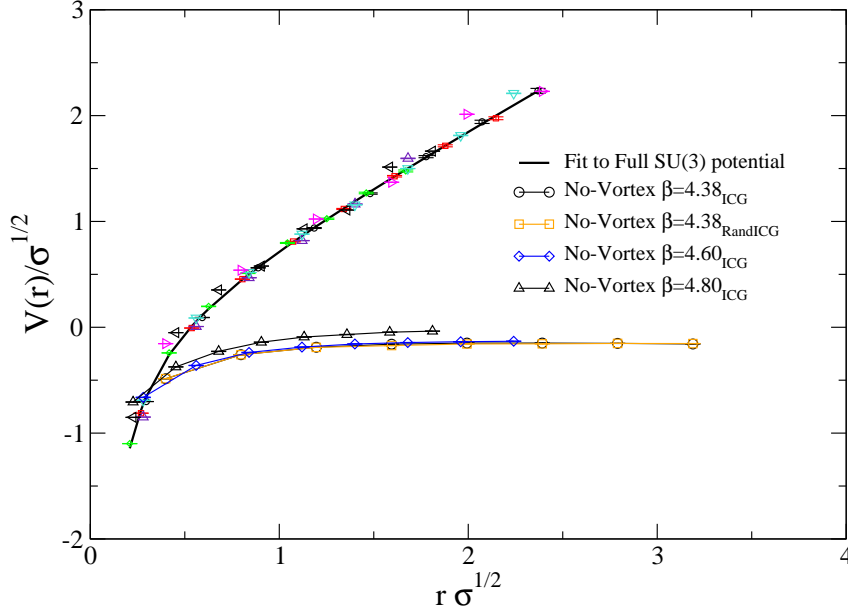
Figure 4.9: Static quark-antiquark potential for the ICG vortex-removed theory. The full SU(3) gauge theory is plotted for comparison. No significant difference between MCG (fig. 4.7) and ICG potentials is seen. Random start and standard ICG show no difference.

This phase is incorporated into the Wilson-loop expectation value in the following way, for details please refer to appendix B.1:

$$\langle W(\mathcal{C}) \rangle = (1 - 3p) \left\langle \tilde{W}_0(\mathcal{C}) \right\rangle \exp[-\kappa A], \tag{4.9}$$

$$\exp[-\sigma A] = \exp[-(\sigma_{cp} + \kappa)A] \left\langle \tilde{W}_0(\mathcal{C}) \right\rangle, \tag{4.10}$$

with p being the probability that a vortex flux of $m = +1$ flows through a Wilson-loop, σ being the full string tension and σ_{cp} being the string tension of the vortex-only theory. The missing string tension will then be represented by κ. $\langle W(\mathcal{C}) \rangle$ being the expectation value for the full theory and $\left\langle \tilde{W}_0(\mathcal{C}) \right\rangle$ being the expectation value for Wilson-loops having the center flux 0.

Eq. 4.10 shows a possibility of how the phenomenon of the missing string tension in the vortex-only theory combined with the vanishing string tension in the vortex-removed theory could be explained. However, it is completely unclear at the

β	σ_{Full}	σ_{MCGVort}	$\sigma_{\text{MCGNo-Vort}}$	σ_{ICGVort}	$\sigma_{\text{ICGNo-Vort}}$
4.38	100	62	0	56/52	0/0
4.53	100	66	0	n.a.	n.a.
4.60	100	61	0	58	0
4.80	100	61	5	58	5

Table 4.1: String tension for vortex-only and vortex-removed theories, both for MCG and ICG, in percentage of the full SU(3) string tension. MCG vortex-only theory yields slightly larger values. The second values for $\beta = 4.38$ ICG are for the random start method. Values are approximations.

moment how the κ-parameter can be related to physics. A second drawback in this method is that neither the numerical value of the missing string tension can be explained, nor why there is no missing string tension in LCG, for which a similar calculation can be performed. Nevertheless, this shows that the missing string tension can be incorporated into the center vortex picture. In principle one could even do calculations on the lattice in order to find the value of κ. One just needs to calculate Wilson-loop expectation values $\langle W(\mathcal{C}) \rangle$ for the full theory and for Wilson-loops $\langle W_{-,0,+}(\mathcal{C}) \rangle$ having center flux $m = -1, 0, 1$ separately and determine κ via eq. 4.10. In practice, however, it is too costly to determine the Wilson-loops to the accuracy needed for a calculation of κ.

4.7   Laplacian Center Gauge

A second possibility to deal with the missing string tension is not to use MCG for gauge fixing, but to use a different gauge – the Laplacian center gauge (LCG).

For technical details about the LCG procedure please refer to [51]. A very brief outline of the procedure follows.
The functional R_{mes} (eq. 2.26) can be rewritten as

$$R_{\text{mes}} = \frac{1}{N_l} \sum_{x,\mu} \frac{1}{N^2} \left[\text{Tr} O^T(x) R_\mu(x) O(x+\mu) + 1 \right], \qquad (4.11)$$

with the adjoint matrices being defined by

$$O^{ab}(x) = 2\text{Tr} \left\{ t^a \Omega(x) t^b \Omega^\dagger(x) \right\}, \quad R_\mu^{ab}(x) = 2\text{Tr} \left\{ t^a U_\mu(x) t^b U_\mu^\dagger(x) \right\}, \quad (4.12)$$

and $t^{a,b}$ being the generators of the SU(N) algebra. Eq. 4.11 can be rewritten as

$$N^2 R_{\text{mes}} = \frac{1}{N_l} \mathcal{O}^T \mathcal{R} \mathcal{O} + 1, \qquad (4.13)$$

where the vector $\mathcal{O}$ of the combined coordinate and colour space $\left\{O^{ab}(x)\right\} \to \mathcal{O}$ has been introduced. $\mathcal{R}$ is the adjoint Laplacian operator, i.e.

$$\mathcal{R}^{ab}_{xy} = \frac{1}{2} \sum_{\mu} \left[R^{ab}_{\mu}(x)\delta_{y,x+\mu} + R^{ba}_{\mu}(x-\mu)\delta_{y,x-\mu} \right] , \qquad (4.14)$$

which is up to a term proportional to the unit matrix. The vector $\mathcal{O}$ is constrained by the set of vectors n^a with $O_{ab} = \left\{n^1(x), n^2(x), n^3(x)\right\}_{ab}$ being orthonormal. For the gauge fixing these constraints are relaxed and the $N-1$ largest eigenvalues of the supermatrix $\mathcal{R}$ are found. With the help of Gram-Schidt orthogonalisation the adjoint gauge transformations $O^{ab}(x)$ are then reconstructed from the eigenvectors. It is important to point out that the LCG procedure also seeks to maximise the *mesonic* gauge condition. However, due to the re-orthogonalisation of the eigenvectors, the value for the overlap R_{mes} achieved with LCG is significantly smaller than the one achieved with MCG. Simulations for LCG were performed for $\beta = 4.38, 4.60$ and 4.80 using the same improved configurations, kindly provided by the CSSM lattice collaboration, as for MCG.
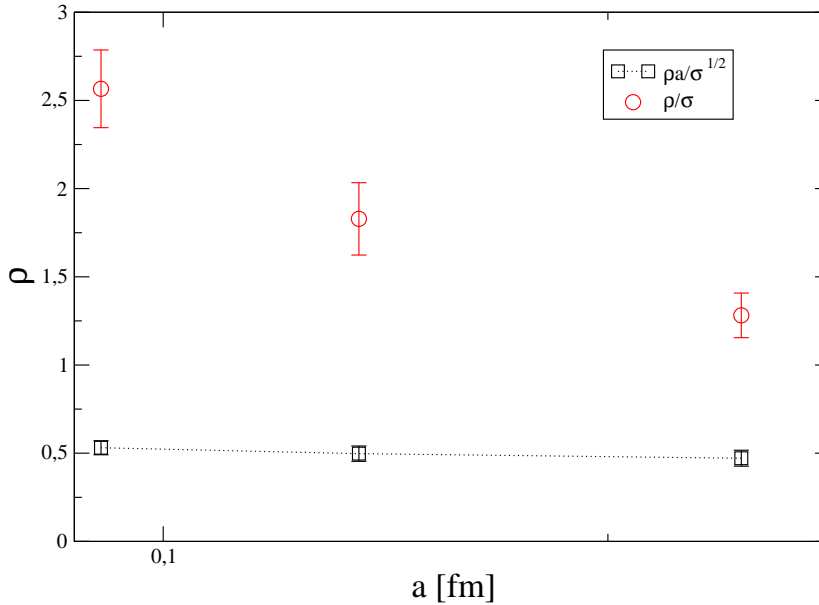

Figure 4.10: The LCG vortex density in physical units ρ/σ and scaled with $a\sqrt{\sigma}$ is plotted. $\rho a/\sqrt{\sigma}$ is independent of the lattice spacing a within errorbars.

A vortex only-theory for LCG has been shown to reproduce the full string tension with the vortex-removed theory having no string tension [51, 23]. However LCG has the drawback that the vortex density diverges in the continuum limit, but in some controlled way. For LCG not the physical vortex density $\rho_{\mathrm{phys}} = \rho_{\mathrm{lat}}/a^2\sigma$, but the quantity $\rho_{\mathrm{lat}}/a\sqrt{\sigma}$ is almost independent of the lattice spacing [23]. There is only a very small rise seen in fig. 4.10. It is not clear at the moment why this is the case and how the vortices found in LCG can be related to physical vortices. No speculations about any possibilities will be done here, but the example of LCG should stress out that it is possible to get a vortex-only and vortex-removed theory with full and vanishing string tension respectively.

Chapter 5

Conclusions

5.1 Low-lying eigenmodes concluded

This work showed that not only zero modes, but all low-lying eigenmodes of the hermitian Wilson-Dirac operator D_W are strongly correlated to topological objects for $\kappa \geq \kappa_\mathrm{c}$. These objects can be instantons for which $\mathrm{S}/\mathrm{S}_0 = \mathrm{Q}$, $\mathrm{Q} \in \mathcal{Z}$, or topological fluctuations with $\mathrm{S}/\mathrm{S}_0 > \mathrm{Q}$. One eigenmode is correlated to at least one topological object with correlations to more than one object becoming more likely as eigenvalues become degenerate and eigenmodes become broader in size. For $\kappa < \kappa_\mathrm{c}$ the correlations broaden very quickly and are lost for values smaller than about $(\kappa_\mathrm{c} - 0.02)$. For $\kappa > \kappa_\mathrm{c}$ the correlations become sharper until $\kappa = \kappa_\mathrm{max}$ for which the correlations are strongest. For $\kappa > \kappa_\mathrm{max}$ the correlations broaden again.

Eigenmodes of 12-sweep cooled configurations show a different behaviour depending on whether they belong to eigenvalues on the left or right-hand side of the rhomboid-shaped eigenvalue spectrum of a cooled configuration as seen in fig. 3.5. Eigenmodes belonging to the left-hand side of the eigenvalue spectrum are strongly localised and show the same behaviour as eigenmodes of hot configurations. Eigenmodes belonging to the right-hand side of the eigenvalue spectrum are very weakly localised, but are still correlated to topology. This suggests that those eigenmodes correspond to very high eigenmodes in a hot configuration, which are lowered by cooling.

The value of κ where the weakly localised eigenmodes set in becomes smaller with cooling. This supports the idea of high values of κ corresponding to localisations on small topological objects. Small topological objects are removed first under improved cooling thus eigenmodes for high values of κ are the first ones to loose the strong localisation.

When an instanton model is fitted to the eigenmode density, using eq. (2.13), and to the topological charge density, using eq. (2.12), strongly localised eigenmodes

have about the same size for ρ as the correlated topological objects. For κ_{max} eigenmodes are slightly smaller than the correlated topological objects and for κ smaller than $\kappa \approx \kappa_{\mathrm{max}} - 0.02$ eigenmodes are slightly larger.

On a single instanton configuration the correlation to the instanton persists strongly only for the lowest eigenmode and is then gradually lost for higher eigenmodes. On SU(3) background fields correlation for the 20 lowest eigenmodes is seen. There is only little broadening which suggests that the correlations will persist for eigenmodes higher than 20.

For hot configurations these correlations allow to "see through" the noise to underlying topological objects. This enables one to track the movement of these objects as a function of cooling.

5.2   Conclusions and outlook for the vortex picture

This work showed that the phase distribution of large Wilson-loops for full Monte-Carlo generated SU(3) lattice configurations is strongly peaked at values of $\phi_m = \frac{2\pi}{3}m$ with $m = -1, 0, 1$. This corresponds to the center elements of SU(3). It indicates that large Wilson-loops are center dominated. Thus center degrees of freedom, i.e. center vortices, are important objects if one examines physical properties via Wilson-loops. The confining capability examined in this work is a good example for such a degree of freedom.

Different methods exist to identify degrees of freedom which might give a picture about confinement. With the help of three constraints

- (i) the degrees of freedom are sensible in the continuum limit,

- (ii) they are connected to confinement,

- (iii) they are weakly interacting,

one can choose the right method. If one chooses a center vortex degree of freedom, criterium (ii) is immediately satisfied [25]. One now has to choose between different methods of center vortex identification. With the help of the remaining criteria one can find a suitable method. The procedure chosen to start with, namely gauge fixing to MCG using the *mesonic* gauge condition (eq. 2.26) followed by center projection, satisfies both remaining constraints. The MCG vortex density is found to be independent of the lattice spacing a. With a value of $\rho_\emptyset = 1.97(14)\mathrm{fm}^{-2}$ it is close to the random vortex value, thus a weak interaction according to the random vortex model is possible.

In order to find out more about the confining properties of such vortices in SU(3) LGT the static quark-antiquark potential has been calculated for the full, the

vortex-only and the vortex-removed theory. After removing the vortices the string tension vanishes for lattices with a large enough physical volume, leading to a non-confining theory. My finding is that the volume should be at least $(1.49\,\mathrm{fm})^3 \times 3.35\,\mathrm{fm}$, corresponding to a $16^3 \times 32$ lattice with $\beta = 4.60$. On the other hand, a vortex-only theory recovers about 62% of the full string tension. This is contrary to SU(2) LGT, where the full string tension is recovered by the vortex-only theory. Further analysis was done to find an explanation for the missing string tension. The first idea was to test if the use of the *ideal* gauge condition (eq. 2.24) implied with an iteration overrelaxation algorithm resolves the puzzle of the missing string tension. Even with the, compared to MCG higher, vortex density of $\rho_\emptyset = 5.04(15)\mathrm{fm}^{-2}$ the vortices identified with this ICG procedure still have the desired properties. However this gauge condition again yields not the full string tension, but only about 58% of the full string tension in a vortex-only theory. This shows that the mesonic gauge condition yields, for practical use, a satisfying overlap between center elements $Z_\mu(x)$ and links $U_\mu^\Omega(x)$. Neither mesonic, nor ideal gauge condition yield the full string tension for the vortex-only case, but both give almost zero string tension for the vortex-removed theory. Greensite and Olejnik [50] showed that this at first sight puzzling result could be incorporated in the center vortex picture by introducing an additional phase κ. Unfortunately this is only a proof of principle, it is not clear if there is any physical meaning behind this parameter. A calculation to clarify this, although possible in principle, is not feasible at the moment due to the noise in large Wilson-loops.

On the way of finding some other gauge condition, which could lead to full string tension, an old friend – the Laplacian Center Gauge – has been proposed. Contrary to MCG and ICG gauges discussed above LCG vortex-only and vortex-removed theories yield full and zero string tension respectively. However, there is one drawback, the physical vortex density $\rho_\mathrm{phys} = \rho_\mathrm{lat}/a^2\sigma$ diverges in the continuum limit. But this divergence happens in a controlled way. The quantity $\rho_\mathrm{lat}/a\sqrt{\sigma}$ is independent of the lattice spacing a. Unfortunately this behaviour is not yet understood.

The confinement problem in lattice QCD is still an unsolved, but very exciting problem. The center vortex ansatz has promising properties with physical vortices for MCG and full SU(3) string tension in a vortex-only theory for LCG. More work to gain a deeper understanding of the vortex texture making it possible to combine those desired properties in one simple procedure and allowing a physical insight into the confinment problem is still necessary. I hope however, that this work helped to put some small pieces in the big puzzle of quark properties, topology and confinement.

Appendix A

Useful tools

A.1 Conversion of physical units

Throughout this work natural units, $\hbar = c = k_B = 1$, are used. Thus energy and mass have the dimension of inverse length. The scale for conversion of lattice units in physical ones is set by $\sqrt{\sigma} = 440$ MeV. This converts into a length via

$$1\text{fm} \approx 5.1 \cdot 10^{-3} \frac{1}{\text{MeV}}. \tag{A.1}$$

A.2 Wilson-loop

I define the Wilson-loops to include the trace. A 1×1 Wilson-loop is then given by,

$$W_{\mu\nu} = \frac{1}{3}\text{Tr}[U_\mu(x)U_\nu(x+\mu)U_\mu^\dagger(x+\nu+\mu)U_\nu^\dagger(x)], \tag{A.2}$$

with $U_\mu(x) \in \text{SU}(3)$ being the link variables.

A.3 Pauli Matrices

$$\sigma_1 = \begin{pmatrix} 0 & 1 \\ 1 & 0 \end{pmatrix} \tag{A.3}$$

$$\sigma_2 = \begin{pmatrix} 0 & -i \\ i & 0 \end{pmatrix} \tag{A.4}$$

$$\sigma_3 = \begin{pmatrix} 1 & 0 \\ 0 & -1 \end{pmatrix} \tag{A.5}$$

A.4   Gamma Matrices

The gamma matrices in chiral basis are used for this work,

$$\gamma_0 = \begin{pmatrix} 0 & i\mathbb{1}_2 \\ -i\mathbb{1}_2 & 0 \end{pmatrix}, \tag{A.6}$$

$$\gamma_i = \begin{pmatrix} 0 & \sigma_i \\ \sigma_i & 0 \end{pmatrix}, \qquad i = 1, 2, 3, \tag{A.7}$$

$$\gamma_5 = \begin{pmatrix} \mathbb{1}_2 & 0 \\ 0 & -\mathbb{1}_2 \end{pmatrix}, \tag{A.8}$$

with σ_i being the Pauli matrices and $\gamma_4 = \gamma_0$.
The following relations hold for the gamma matrices,

$$\mathrm{Tr}\,\gamma_\mu = 0, \tag{A.9}$$

$$\{\gamma_\mu, \gamma\nu\} = 2\delta_{\mu\nu}\mathbb{1}_4, \tag{A.10}$$

and

$$\{\gamma_\mu, \gamma_5\} = 0. \tag{A.11}$$

Appendix B

Calculations

B.1 Greensite-Olejnik Hypothesis

In this section I will perform the explicit calculation of Jeff Greensite's and Stefan Olejnik's idea [50] how to incorporate the missing string tension in the center vortex picture.

The relation between Wilson-loop expectation value and the string tension for a full and for a vortex only theory are,

$$\langle W(\mathcal{C}) \rangle = \exp[-\sigma A], \tag{B.1}$$

$$\langle Z(\mathcal{C}) \rangle = \exp[-\sigma_{cp} A] = (1 - 3p), \tag{B.2}$$

with p being the probability that a vortex flux of $+1$ flows through a Wilson-loop, corresponding to $\langle W(\mathcal{C}) \rangle = \exp[i\frac{2\pi}{3}]$. Inside the expectation value the Wilson-loop can always be factorised in a center part and a rest.

$$
\begin{aligned}
\langle W(\mathcal{C}) \rangle &= \left\langle Z(\mathcal{C}) \tilde{W}(\mathcal{C}) \right\rangle \\
&= p \exp[-\frac{2\pi i}{3}] \left\langle \tilde{W}_+(\mathcal{C}) \right\rangle + p \exp[+\frac{2\pi i}{3}] \left\langle \tilde{W}_-(\mathcal{C}) \right\rangle \\
&\quad + (1 - 2p) \mathbb{1} \left\langle \tilde{W}_-(\mathcal{C}) \right\rangle.
\end{aligned}
\tag{B.3}
\tag{B.4}
$$

With $\exp[+\frac{2\pi i}{3}] = -\exp[+\frac{\pi i}{3}]$ and $\exp[+\frac{2\pi i}{3}] \left\langle \tilde{W}_-(\mathcal{C}) \right\rangle$ being the hermitian conjugate of $\exp[-\frac{2\pi i}{3}] \left\langle \tilde{W}_+(\mathcal{C}) \right\rangle$ one gets

$$\langle W(\mathcal{C}) \rangle = (1 - 2p) \left\langle \tilde{W}_-(\mathcal{C}) \right\rangle - 2p \mathrm{Re} \left(-\exp[+\frac{\pi i}{3}] \left\langle \tilde{W}_+(\mathcal{C}) \right\rangle \right). \tag{B.5}$$

$\left\langle \tilde{W}_+(\mathcal{C}) \right\rangle$ can be written as $\left\langle \tilde{W}_+(\mathcal{C}) \right\rangle = \left\langle \tilde{W}_0(\mathcal{C}) \right\rangle + \Delta W$. Inserted into eq. B.5 this yields

$$
\begin{aligned}
\cdots &= (1-2p)\left\langle \tilde{W}_0(\mathcal{C}) \right\rangle - 2p\mathrm{Re}\left(\exp[-\frac{\pi i}{3}]\left\langle \tilde{W}_0(\mathcal{C}) \right\rangle + \exp[-\frac{\pi i}{3}]\Delta W \right) \\
&= (1-3p)\left\langle \tilde{W}_0(\mathcal{C}) \right\rangle - 2p\mathrm{Re}\left(\exp[-\frac{\pi i}{3}]\Delta W \right).
\end{aligned}
\tag{B.6}
$$

With $2p\mathrm{Re}\left(\exp[-\frac{\pi i}{3}]\Delta W \right) = p\delta\tilde{W}$ and the positivity of the Wilson loop expectation value,

$$
p\delta\tilde{W} < (1-3p)\left\langle \tilde{W}_0(\mathcal{C}) \right\rangle,
\tag{B.7}
$$

is valid. If one then assumes that $p\delta\tilde{W}$ is only exponentially smaller than $(1-3p)\left\langle \tilde{W}_0(\mathcal{C}) \right\rangle$, $p\delta\tilde{W}$ can be written as,

$$
p\delta\tilde{W} = (1-3p)\left\langle \tilde{W}_0(\mathcal{C}) \right\rangle (1-\exp[-\kappa A]).
\tag{B.8}
$$

Inserting eq. B.8 in eq. B.6 one gets for the Wilson loop expectation value

$$
\begin{aligned}
\langle W(\mathcal{C}) \rangle &= (1-3p)\left\langle \tilde{W}_0(\mathcal{C}) \right\rangle \exp[-\kappa A], \\
\exp[-\sigma A] &= \exp[-(\sigma_{cp}+\kappa)A]\left\langle \tilde{W}_0(\mathcal{C}) \right\rangle,
\end{aligned}
\tag{B.9}
\tag{B.10}
$$

with σ being the full string tension and σ_{cp} being the string tension of the vortex-only theory. This is equation 4.10 as given in sec. 4.6.

Appendix C

Code overview

A big part of work done in the field of lattice gauge theory is code development. This appendix gives a short overview of the modules developed for this diploma thesis. Questions about and requests for the source code are welcome at djkuster@tphys.physik.uni-tuebingen.de.

All of the modules were developed in Fortran90, with special High Performance Fortran extensions used for modules designed for the Orion supercomputer.

C.1 Low-lying eigenmodes codes

Production for the low-lying eigenmodes part of this work was done one the Orion supercomputer, courtesy to the Center for Subatomic Structure of Matter (CSSM), the South Australian Partnership for Advanced Computing (SAPAC) and the National Computing Facility for Lattice Gauge Theory. Orion is a SUN Technical Compute Farm with 40 nodes. The code was parallelised with the help of High Performance Fotran and MPI.

C.1.1 Lanczos type eigenvalue solver

Routine for finding eigenvalues of Dirac matrices. This routine was later discarded for a conjugate gradient routine. Lanczos is not parallelisable and does not yield eigenvectors.

C.1.2 Conjugate gradient eigenvalue and -vector routine

Main advantage of a conjugate gradient routine is its parallelisability and that it yields eigenvalues *and* eigenvectors. The main routine was written by Waseem Kamleh and modified by myself to yield the eigenvector norms.

C.1.3   Instanton fitting routine

Fits an instanton (see eq. 2.12 and eq. 2.13), depending on whether the object to be fitted is topological charge, or eigenmode density. Yields size and location of the object.

C.2   Vortex codes

Production for the vortex part of this work was done on the CIP computer pool at the Institut für Theoretische Physik, Universität Tübingen. The code is purely written in Fortran90.

C.2.1   MCG gauge fixing routine

Gauge fixes a Monte-Carlo generated SU(3) lattice configuration to MCG by maximising R_{mes} given by eq. 2.26. All technical details about maximal center gauge fixing in SU(3) are to be found in sec. 2.4.1.

C.2.2   ICG gauge fixing routine

Gauge fixes a previously MCG gauge fixed SU(3) lattice configuration to ICG by an iteration overrelaxation procedure, which maximises R_{ideal} given by eq. 2.24. For more details on the procedure see sec. 4.5.

C.2.3   Vortex identification and removal

Several small subroutines find the closest center element $Z_\mu(x)$ for each link $U_\mu(x)$ on gauge fixed configurations, identify plaquettes which are pierced by a vortex, calculate the corresponding vortex density and remove the vortices. The configurations $\{Z_\mu\}$ are written out as vortex-only configuration and the $\{Z_\mu^\dagger U_\mu\}$ configurations are written out as vortex-removed configurations.

C.2.4   Wilson loops

A subroutine calculating $n \times m$ Wilson-loops with

$$
\begin{aligned}
W_{\mu\nu} \;=\; & \frac{1}{3}\mathrm{Tr}[U_\mu(x)\cdots U_\mu(x+(n-1)\mu)U_\nu(x+n\mu)\cdots \\
& U_\nu(x+n\mu+(m-1)\nu)U_\mu^\dagger(x+m\nu+(n-1)\mu)\cdots \\
& U_\mu^\dagger(x+m\nu)U_\nu^\dagger(x+(m-1)\nu)\cdots U_\nu^\dagger(x)],
\end{aligned}
\tag{C.1}
$$

With $U_\mu(x) \in \mathrm{SU}(3)$ being the link variables. This subroutine is used for checking the Greensite-Olejnik hypothesis and for calculating the static quark-antiquark potential.

C.2.5 $q\bar{q}$-potential

Main analysis tool for vortex-only and vortex-removed configurations. Uses the overlap enhancement and fitting method described in sec. 2.5. Vortex-only configurations are not overlap enhanced.
A subroutine of this program fits the function

$$V_{\mathrm{lat}} = \sigma R - \frac{b}{R} + V_0 \tag{C.2}$$

to the data and calculates the points for the potential V_{phys} in physical units.

$$V_{\mathrm{phys}}(r) = \frac{V_{\mathrm{lat}} - V_0}{\sqrt{\sigma}}, \tag{C.3}$$

with $r = R\sqrt{\sigma}$. In this way not only the potential, but also the string tension σ is found.

C.2.6 Vortex Visualisation plotfile routine

This routine tracks all vortices via a recursive subroutine. It writes out coordinates for each point, where a plaquette is pierced by a vortex. Plotfiles created in this way can the be used to do a visualisation of center vortices on the lattice. The visualisations themselves were kindly done by Derek Leinweber with Advanced Visual Express (AVS)[1].

---

[1]http://www.avs.com

List of Figures

List of Tables

Bibliography

[1] I. Montvay and G. Münster. *Quantum Fields on a Lattice*. Cambridge University Press, 1997.

[2] H. J. Rothe. *Lattice Gauge Theories - An Introduction*. World Scientific, 1992.

[3] Holger Bech Nielsen and M. Ninomiya. No go theorem for regularizing chiral fermions. *Phys. Lett.*, B105:219, 1981.

[4] Rajamani Narayanan and Herbert Neuberger. A construction of lattice chiral gauge theories. *Nucl. Phys.*, B443:305–385, 1995.

[5] Herbert Neuberger. A practical implementation of the Overlap-Dirac operator. *Phys. Rev. Lett.*, 81:4060–4062, 1998.

[6] Dmitri Diakonov and V. Yu. Petrov. A theory of light quarks in the instanton vacuum. *Nucl. Phys.*, B272:457, 1986.

[7] Tom Banks and A. Casher. Chiral symmetry breaking in confining theories. *Nucl. Phys.*, B169:103, 1980.

[8] Thomas DeGrand and Anna Hasenfratz. Low-lying fermion modes, topology and light hadrons in quenched QCD. *Phys. Rev.*, D64:034512, 2001.

[9] Robert G. Edwards, Urs M. Heller, and Rajamani Narayanan. Spectral flow, chiral condensate and topology in lattice QCD. *Nucl. Phys.*, B535:403–422, 1998.

[10] Robert G. Edwards, Urs M. Heller, and Rajamani Narayanan. The hermitian Wilson-Dirac operator in smooth SU(2) instanton backgrounds. *Nucl. Phys.*, B522:285–297, 1998.

[11] D. Smith, H. Simma, and M. Teper. Topological structure of the SU(3) vacuum and exceptional eigenmodes of the improved Wilson-Dirac operator. *Nucl. Phys. Proc. Suppl.*, 63:558–560, 1998.

[12] K. Jansen, C. Liu, H. Simma, and D. Smith. Low-lying eigenvalues of the Wilson-Dirac operator. *Nucl. Phys. Proc. Suppl.*, 53:262–265, 1997.

[13] Daniel-Jens Kusterer, John Hedditch, Waseem Kamleh, Derek B. Leinweber, and Anthony G. Williams. Low-lying eigenmodes of the Wilson-Dirac operator and correlations with topological objects. *Nucl. Phys.*, B628:253–269, 2002.

[14] Thomas Kalkreuter and Hubert Simma. An accelerated conjugate gradient algorithm to compute low lying eigenvalues: A study for the Dirac operator in SU(2) lattice QCD. *Comput. Phys. Commun.*, 93:33–47, 1996.

[15] A. Jaffe and E. Witten. Quantum Yang-Mills Theory.

[16] G. 't Hooft. Topology of the gauge condition and confinement phases in nonabelian gauge theories. *Nucl. Phys.*, B190:455, 1981.

[17] K. Langfeld, H. Reinhardt, and A. Schäfke. Center vortex properties in the Laplace center gauge of SU(2) Yang-Mills theory. *Phys. Lett.*, B504:338–344, 2001.

[18] M. Engelhardt, K. Langfeld, H. Reinhardt, and O. Tennert. Deconfinement in SU(2) Yang-Mills theory as a center vortex percolation transition. *Phys. Rev.*, D61:054504, 2000.

[19] M. Faber, J. Greensite, S. Olejnik, and D. Yamada. Some insights into the method of center projection. *Nucl. Phys. Proc. Suppl.*, 83:527–529, 2000.

[20] L. Del Debbio, M. Faber, J. Greensite, and S. Olejnik. Center dominance and Z(2) vortices in SU(2) lattice gauge theory. *Phys. Rev.*, D55:2298–2306, 1997.

[21] C. Alexandrou, P. de Forcrand, and M. D'Elia. The role of center vortices in QCD. *Nucl. Phys.*, A663:1031–1034, 2000.

[22] Manfried Faber, Jeff Greensite, and Stefan Olejnik. First evidence for center dominance in SU(3) lattice gauge theory. *Phys. Lett.*, B474:177–181, 2000.

[23] Kurt Langfeld. Vortex matter in SU(3) lattice gauge theory. *Phys. Rev.*, D69:014503, 2004.

[24] J. D. Stack, W. W. Tucker, and R. J. Wensley. The maximal abelian gauge, monopoles, and vortices in SU(3) lattice gauge theory. *Nucl. Phys.*, B639:203–222, 2002.

[25] J. Greensite. The confinement problem in lattice gauge theory. *Prog. Part. Nucl. Phys.*, 51:1, 2003.

[26] L. Del Debbio, M. Faber, J. Giedt, J. Greensite, and S. Olejnik. Detection of center vortices in the lattice yang-mills vacuum. *Phys. Rev.*, D58:094501, 1998.

[27] K. G. Wilson and A. (ed.) Zichichi. *New Phenomena in Subnuclear Physics, Part A*. Plenum Press, New York, 1975.

[28] B. Sheikholeslami and R. Wohlert. Improved continuum limit lattice action for QCD with Wilson fermions. *Nucl. Phys.*, B259:572, 1985.

[29] Martin Lüscher, Stefan Sint, Rainer Sommer, and Peter Weisz. Chiral symmetry and O(a) improvement in lattice QCD. *Nucl. Phys.*, B478:365–400, 1996.

[30] Philippe de Forcrand, Margarita Garcia Perez, and Ion-Olimpiu Stamatescu. Topology of the SU(2) vacuum: A lattice study using improved cooling. *Nucl. Phys.*, B499:409–449, 1997.

[31] S. Bilson-Thompson, F. D. R. Bonnet, D. B. Leinweber, and Anthony G. Williams. Cooling for instantons and the wrath of Nahm. *Nucl. Phys. Proc. Suppl.*, 109:116–120, 2002.

[32] Sundance O. Bilson-Thompson, Derek B. Leinweber, and Anthony G. Williams. Highly-improved lattice field-strength tensor. *Ann. Phys.*, 304:1–21, 2003.

[33] Frederic D. R. Bonnet, Derek B. Leinweber, Anthony G. Williams, and James M. Zanotti. Improved smoothing algorithms for lattice gauge theory. *Phys. Rev.*, D65:114510, 2002.

[34] Robert G. Edwards, Urs M. Heller, and Rajamani Narayanan. A study of practical implementations of the Overlap-Dirac operator in four dimensions. *Nucl. Phys.*, B540:457–471, 1999.

[35] Christof Gattringer, Meinulf Gockeler, C. B. Lang, P. E. L. Rakow, and Andreas Schafer. Comparing lattice Dirac operators in smooth instanton backgrounds. *Phys. Lett.*, B522:194–200, 2001.

[36] Alvaro Montero. Study of SU(3) vortex-like configurations with a new maximal center gauge fixing method. *Phys. Lett.*, B467:106–111, 1999.

[37] Kurt Langfeld. Vortex critical behavior at the de-confinement phase transition. *Phys. Rev.*, D67:111501, 2003.

[38] H. Reinhardt, M. Engelhardt, K. Langfeld, M. Quandt, and A. Schäfke. Mag-
netic monopoles, center vortices, confinement and topology of gauge fields.
[arXiv:hep-th/9911145], 1999.

[39] Tamas G. Kovacs and E. T. Tomboulis. Vortices and the SU(3) string tension.
Phys. Lett., B443:239–243, 1998.

[40] Nicola Cabibbo and Enzo Marinari. A new method for updating SU(N) ma-
trices in computer simulations of gauge theories. *Phys. Lett.*, 119B:387–390,
1982.

[41] J. D. Stack. The heavy quark potential. In *Argonne 1984, Proceedings,
Gauge Theory On A Lattice: 1984*, 131-137.

[42] Gunnar S. Bali and Klaus Schilling. Running coupling and the lambda pa-
rameter from SU(3) lattice simulations. *Phys. Rev.*, D47:661–672, 1993.

[43] G. S. Bali and K. Schilling. Static quark - anti-quark potential: Scaling
behavior and finite size effects in SU(3) lattice gauge theory. *Phys. Rev.*,
D46:2636–2646, 1992.

[44] Philippe de Forcrand, Margarita Garcia Perez, James E. Hetrick, and Ion-
Olimpiu Stamatescu. Topological properties of the QCD vacuum at T = O
and T approx. T(c). *[arXiv:hep-lat/9802017]*, 1997.

[45] D.-J. Kusterer. Eigenmodes project visualization. http://homepages.uni-
tuebingen.de/student/daniel-jens.kusterer/phi/.

[46] Herbert Neuberger. Bounds on the Wilson Dirac operator. *Phys. Rev.*,
D61:085015, 2000.

[47] Pilar Hernandez, Karl Jansen, and Martin Lüscher. Locality properties of
Neuberger's lattice Dirac operator. *Nucl. Phys.*, B552:363–378, 1999.

[48] W. Kamleh, D. J. Kusterer, D. B. Leinweber, and A. G. Williams. Flic-overlap
fermions and topology. *Nucl. Phys. Proc. Suppl.*, 119:828–830, 2003.

[49] D.-J. Kusterer, W. Kamleh, D. B. Leinweber, and A. G. Williams. Low-lying
eigenmodes of FLIC and fat-link Wilson actions. to be submitted.

[50] Jeff Greensite and Stefan Olejnik. private communication.

[51] P. de Forcrand and M. Pepe. Center vortices and monopoles without lattice
gribov copies. *Nucl. Phys.*, B598:557–577, 2001.

[52] H. Fischer and H. Kaul. *Mathematik für Physiker 1*. Teubner, Stuttgart, third edition, 1997.

[53] H. Fischer and H. Kaul. *Mathematik für Physiker 2*. Teubner, Stuttgart, 1998.

[54] I. N. Bronstein, K. A. Semendajew, G. Musiol, and H. Mühlig. *Taschenbuch der Mathematik*. Verlag Harri Deutsch, Frankfurt/Main, fourth edition, 1999.

[55] Carlo Rovelli. A dialog on quantum gravity. *Int. J. Mod. Phys.*, D12:1509–1528, 2003.

Erklärung

Hiermit erkläre ich, dass die vorliegende Diplomarbeit von mir selbständig verfasst worden ist. Dabei habe ich keine anderen als die angegebenen Quellen und Hilfsmittel verwendet.

Tübingen, den 18.03.2004